



**HAL**  
open science

# Weak lensing survey of galaxy clusters in the CFHTLS Deep

Raphael Gavazzi, Genevieve Soucail

► **To cite this version:**

Raphael Gavazzi, Genevieve Soucail. Weak lensing survey of galaxy clusters in the CFHTLS Deep. 2006. hal-00071677v1

**HAL Id: hal-00071677**

**<https://hal.science/hal-00071677v1>**

Preprint submitted on 23 May 2006 (v1), last revised 6 Nov 2006 (v3)

**HAL** is a multi-disciplinary open access archive for the deposit and dissemination of scientific research documents, whether they are published or not. The documents may come from teaching and research institutions in France or abroad, or from public or private research centers.

L'archive ouverte pluridisciplinaire **HAL**, est destinée au dépôt et à la diffusion de documents scientifiques de niveau recherche, publiés ou non, émanant des établissements d'enseignement et de recherche français ou étrangers, des laboratoires publics ou privés.

# Weak lensing survey of galaxy clusters in the CFHTLS Deep<sup>★</sup>

R. Gavazzi<sup>1</sup> and G. Soucail<sup>1</sup>

Laboratoire d'Astrophysique de Toulouse-Tarbes, Observatoire Midi-Pyrénées, UMR5572 CNRS & Université Paul Sabatier, 14 Avenue Edouard Belin, 31400 Toulouse, France

Received sometime; accepted later

## ABSTRACT

**Aims.** We present a weak lensing search of galaxy clusters in the 4 deg<sup>2</sup> of the CFHT Legacy Survey Deep. This work aims at building a mass-selected sample of clusters with well controlled selection effects. This present survey is a preliminary step toward a full implementation in the forthcoming 170 deg<sup>2</sup> of the CFHTLS Wide survey.

**Methods.** We use the deep *i'* band images observed under subarcsecond seeing conditions to perform weak lensing mass reconstructions and to identify high convergence peaks. Thanks to the availability of deep *u\*g'r'i'z'* exposures, sources are selected from their photometric redshifts in the weak lensing analysis. We also use lensing tomography to derive an estimate of the lens redshift. After considering the raw statistics of peaks we check whether they can be associated to a clear optical counterpart or to published X-ray selected clusters.

**Results.** Among the 14 peaks found above a signal-to-noise detection threshold  $\nu = 3.5$ , eight are secure detections with estimated redshift  $0.15 \lesssim z_l \lesssim 0.6$  and a velocity dispersion  $450 \lesssim \sigma_v \lesssim 600 \text{ km s}^{-1}$ . This low mass range is accessible thanks to the high density of background sources. We also use photometric redshifts of sources to test the effect of contamination by source-lens clustering for clusters detection. This latter turns out to play a minor role in our cluster sample. Considering the intersection between the shear-selected clusters and XMM/LSS X-ray clusters in the D1 field, we observe that the ICM gas in these low-mass clusters ( $T_X \sim 1 - 2 \text{ keV}$ ) is not hotter than the temperature inferred from shear, this trend being different for published massive clusters. A more extended weak lensing survey, with higher statistics of mass structures will be a promising way to bypass several of the problems related to standard detection methods based on the complex physics of baryons.

**Key words.** Gravitational lensing – Galaxies: clusters: general – Cosmologie: Large-scale structure

## 1. Introduction

In the context of hierarchical structure formation within the Lambda Cold Dark Matter paradigm ( $\Lambda$ CDM), clusters of galaxies are the very latest structures to assemble. They are also the most extended gravitationally bound systems in the Universe and constitute a key laboratory for cosmology. The time evolution of clusters as well as their abundance and spatial clustering properties are essentially driven by gravity sourced by the CDM mass content (*e.g.* Eke et al. 1996; Haiman et al. 2001; Borgani & Guzzo 2001).

Send offprint requests to: Raphaël Gavazzi, e-mail: rgavazzi@ast.obs-mip.fr

<sup>★</sup> Based on observations obtained with MegaPrime/MegaCam, a joint project of CFHT and CEA/DAPNIA, at the Canada-France-Hawaii Telescope (CFHT) which is operated by the National Research Council (NRC) of Canada, the Institut National des Science de l'Univers of the Centre National de la Recherche Scientifique (CNRS) of France, and the University of Hawaii. This work is based in part on data products produced at TERAPIX and the Canadian Astronomy Data Centre as part of the Canada-France-Hawaii Telescope Legacy Survey, a collaborative project of NRC and CNRS.

Therefore the main physical parameter for a cluster of galaxies is its total mass. However most of observations only have an indirect access to cluster masses and rather measure quantities like the SZ decrement, X-ray or optical/NIR luminosities, the line-of-sight velocity dispersion of the cluster-member galaxies or the temperature of the hot gas in the intra-cluster medium (ICM) from X-ray (*e.g.* Bahcall et al. 1995; Carlberg et al. 1996; Bahcall & Bode 2003; Olsen et al. 1999; Gladders & Yee 2000; Romer et al. 2001; Carlstrom et al. 2002). Hence difficulties arise because one needs well calibrated proxies to convert observables into theoretically relevant quantities like mass and because the process of detecting clusters of galaxies with such indirect methods might suffer various kinds of selection effects. Therefore any attempt to use clusters of galaxies as efficient cosmological probes cannot afford making extensive assessments of the assumed calibration of the scaling laws in the local Universe and at high redshift (*e.g.* Arnaud & Evrard 1999; da Silva et al. 2004; Arnaud et al. 2005).

Gravitational lensing is among the best ways to test biases in the above techniques. The bending of light by intervening

matter along the line of sight from distant sources to the observer only depends on the mass properties of structures without regards of its nature (baryonic or not, luminous or dark) or dynamical state (relaxed or not, hydrostatic equilibrium...). Since the early 90's several groups have reported the detection of a weak lensing signal around massive clusters of galaxies. However the broad range of observational configurations (field of view, depth, seeing, ground- or space-based images, etc) makes difficult a direct comparison of published results. For reviews see Mellier (1999) and Bartelmann & Schneider (2001). Progresses have been made in this direction with weak lensing studies of sizable samples of optically or X-ray selected clusters (Dahle et al. 2002; Cypriano et al. 2004; Clowe et al. 2006; Bardeau et al. 2006). Different mass estimates globally agree although outliers perturb a simple relation between X-ray (or dynamical) and lensing mass estimates (e.g. Allen 1998; Wu 2000; Arabadjis et al. 2004). This suggests that dynamical activity is still important for massive halos and that asphericity and projection effects may complicate both weak lensing and other mass estimates (Metzler et al. 2001; Hoekstra 2003; Clowe et al. 2004; de Putter & White 2005; Gavazzi 2005; De Filippis et al. 2005).

In parallel, the idea of direct detection of galaxy clusters by their weak lensing signal starts to emerge. By measuring the coherent stretching of distant galaxies by intervening structures, one is able to infer the projected density field (i.e. the so-called convergence). Hence high convergence peaks may be identified as massive clusters of galaxies. This is the idea of a direct weak lensing cluster survey (hereafter WLCS), aimed at building a mass-selected cluster sample directly comparable to CDM theory (through N-body cosmological simulations). On the theoretical side, pioneering analytical predictions based on the mass function of halos have been proposed (Schneider 1996; Kruse & Schneider 1999), but they were not able to properly account for projection effects (Reblinsky & Bartelmann 1999). In addition Bartelmann et al. (2001) showed that WLCSs are very sensitive to the details of the clusters density profile. More recently, ray-tracing into N-body cosmological simulations have been used to properly address the critical issue of projections and clusters' asphericity (White et al. 2002; Padmanabhan et al. 2003; Hamana et al. 2004; Tang & Fan 2005) and the way to reduce the effect of noise on cluster detections through an optimised data filtering procedure (Hennawi & Spergel 2005; Maturi et al. 2005; Starck et al. 2006). A step forward will also probably be made with simplified analytical models of the convergence one-point PDF (Taruya et al. 2002; Das & Ostriker 2005). Under standard observational conditions, these works predict that at  $z \sim 0.2$  clusters more massive than  $M \sim 5 \times 10^{13} M_{\odot}$  can be recovered with a signal-to-noise ratio  $\nu = 3$ . This limit drops to  $M \sim 2 \times 10^{14} M_{\odot}$  at  $z \sim 0.7$ . Therefore the main targets of WLCSs are massive clusters of galaxies.

From the point of view of observations, we can mention a few serendipitous detections of galaxies clusters via weak gravitational lensing (e.g. Schirmer et al. 2003, 2004; Dahle et al. 2003). A few examples have also been found to show up through weak lensing techniques without any clear optical counterpart and gave support for the existence for the so-called

“*dark clumps*” (Umetsu & Futamase 2000; Miralles et al. 2002). The practical implementation of a systematic WLCS is however very new. Miyazaki et al. (2002) studied an area of  $2.1 \text{ deg}^2$  with Suprime-Cam on Subaru telescope under excellent seeing conditions. They report an excess of  $4.9 \pm 2.3$  convergence peaks with signal-to-noise  $\nu > 5$ . Hettterscheidt et al. (2005) report the detection of  $\sim 5$  cluster candidates over a set of 50 disconnected VLT/FORS deep images covering an effective area of  $0.64 \text{ deg}^2$  while Wittman et al. (2006) present preliminary results for the first  $8.6 \text{ deg}^2$  of the Deep Lens Survey (eight detections). Haiman et al. (2004) also make interesting predictions for future WLCS applications in the LSST survey.

In this paper we present a weak lensing analysis of the Deep CFHT Legacy Survey<sup>1</sup> covering  $4 \times 1 \text{ deg}^2$  in five optical bands ( $u^*g'r'i'z'$ ) under subarcsec seeing condition as a pilot analysis for the ongoing Wide Survey which will cover  $170 \text{ deg}^2$ . The present work proposes to carry out weak lensing mass reconstructions in the Deep fields and focus on high convergence peaks in order to shed light on WLCS capabilities. The relatively high sample variance of the Deep images prevents any cosmological application of WLCSs but the great depth and amount of photometry make us with an excellent laboratory for a future application to the Wide data.

The paper is organised as follows. In Sect. 2 we briefly review the basics of weak gravitational lensing. In Sect. 3 we present the data at hand, the specific treatment required for weak lensing signal extraction and photometric redshifts. We show mass reconstructions (i.e. convergence maps) in Sect. 4 inferred from the coherent shear field imprinted on distant background sources and from the distribution of foreground early-type galaxies. We also measure the statistics of high convergence peaks whereas we focus on their properties in Sect. 5 by studying the associated optical and X-ray counterparts (when available). We discuss our results in Sect. 6 in the perspective of both cosmology and clusters physics. We resume our main achievements and conclude in Sect. 7.

In the following we assume the “*concordance model*” cosmological background with  $H_0 = 70 \text{ km s}^{-1} \text{ Mpc}^{-1}$ ,  $\Omega_m = 0.3$  and  $\Omega_{\Lambda} = 0.7$ . All magnitudes are expressed in the AB system.

## 2. Basic lensing equations

In this section we briefly summarise the necessary background of gravitational lensing and especially the weak lensing regime which concerns the present analysis. We refer the reader to the reviews of Mellier (1999) and Bartelmann & Schneider (2001) for more detailed accounts.

The fundamental quantity for gravitational lensing is the lens newtonian potential  $\psi(\theta)$  at angular position  $\theta$  which is related to the surface mass density  $\Sigma(\theta')$  projected onto the lens plane through

$$\psi(\theta) = \frac{4G}{c^2} \frac{D_{ol}D_{ls}}{D_{os}} \int d^2\theta' \Sigma(\theta') \ln |\theta - \theta'|, \quad (1)$$

where  $D_{ol}$ ,  $D_{os}$  and  $D_{ls}$  are angular distances to the lens, to the source and between the lens and the source respectively. The

<sup>1</sup> <http://www.cfht.hawaii.edu/Science/CFHTLS/>

deflection angle  $\alpha = \nabla\psi$  relates a point in the source plane  $\beta$  to its image(s) in the image plane  $\theta$  through the lens equation  $\beta = \theta - \alpha(\theta)$ . The local relation between  $\beta$  and  $\theta$  is the Jacobian matrix  $a_{ij} = \partial\beta_i/\partial\theta_j$

$$a_{ij} = \delta_{ij} - \psi_{,ij} = \begin{pmatrix} 1 - \kappa - \gamma_1 & -\gamma_2 \\ -\gamma_2 & 1 - \kappa + \gamma_1 \end{pmatrix}. \quad (2)$$

The convergence  $\kappa(\theta) = \Sigma(\theta)/\Sigma_{\text{crit}}$  is directly related to the surface mass density via the critical density

$$\Sigma_{\text{crit}} = \frac{c^2}{4\pi G} \frac{D_{\text{os}}}{D_{\text{ol}}D_{\text{ls}}}, \quad (3)$$

and satisfies the Poisson equation

$$\Delta\psi = \psi_{,11} + \psi_{,22} = 2\kappa \quad (4)$$

The 2-component shear is  $\gamma = \gamma_1 + i\gamma_2 = \frac{1}{2}(\psi_{,11} - \psi_{,22}) + i\psi_{,12}$  in complex notation. An elliptical object in the image plane is characterised by its complex ellipticity  $e$  defined from the second moments tensor  $Q_{ij}$  of the surface brightness distribution as

$$e = \frac{Q_{11} - Q_{22} + 2iQ_{12}}{Q_{11} + Q_{22} + 2(Q_{11}Q_{22} - Q_{12}^2)^{1/2}} \quad (5)$$

This observed ellipticity can be related to the intrinsic ellipticity of the source  $e_s$  by:

$$e = \begin{cases} \frac{e_s + g}{1 + g^*e_s}, & \text{for } |g| \leq 1 \\ \frac{1 + ge_s^*}{e_s^* + g^*}, & \text{for } |g| > 1 \end{cases} \quad (6)$$

where  $g = \gamma/(1 - \kappa)$  is the so-called reduced shear and  $*$  denotes complex conjugation (Seitz & Schneider 1997; Geiger & Schneider 1998). In the weak lensing regime ( $g \sim \gamma \ll 1$ ), Eq. (6) reduces to  $e = e_s + \gamma$ . Provided the random orientation of the sources reduces the averaged source ellipticity to zero,  $e$  provides an unbiased estimate for the shear  $\gamma$ . The noise associated to this estimator is due to the scatter in the intrinsic ellipticity of sources with a typical value  $\sigma_e \sim 0.3$  per component.

In the equations above we can isolate a geometric term which linearly scales the lensing quantities  $\kappa$ ,  $\psi$ , and  $\gamma$  and only depends on the distance ratio  $D_{\text{ls}}/D_{\text{os}}$ . We thus can write  $\gamma = w(z_1, z_s)\gamma_\infty$  (and so forth for  $\kappa$  and  $\psi$ ) with  $w(z_1, z_s) = D_{\text{ls}}/D_{\text{os}}\Theta(z_s - z_1)$  and  $\Theta(x)$  is the Heavyside step function. If sources are not confined in a thin plane, we account for the distribution in redshift by defining an ensemble average distance factor  $W(z_1)$  such that:

$$W(z_1) = \langle w(z_1, z_s) \rangle_{z_s} = \frac{\int_{z_1}^{\infty} dz_s n(z_s) \frac{D_{\text{ls}}}{D_{\text{os}}}}{\int_0^{\infty} dz_s n(z_s)}. \quad (7)$$

If we now consider a broad distribution of mass intervening between sources and the observer, we can use the Born approximation for the propagation of light in a clumpy Universe

to infer the effective convergence experienced by light bundles:

$$\begin{aligned} \kappa_{\text{eff}}(\theta) &= \int_0^{l_H} \frac{\rho(l, \theta) - \bar{\rho}(l)}{\Sigma_{\text{crit}}(l)} dl \\ &= \frac{3}{2}\Omega_m \left(\frac{H_0}{c}\right)^2 \int_0^{\chi_H} d\chi W(\chi) f_k(\chi) \frac{\delta(f_k(\chi)\theta, \chi)}{a(\chi)}, \end{aligned} \quad (8)$$

with  $l$  (resp.  $\chi$ ) the proper (resp. comoving) distance,  $a$  the scale factor and  $\delta(r)$  the density contrast. At this level we clearly see the projection nature of weak lensing signal. This means that a given  $\kappa$ -peak can be the result of a single  $\delta$ -peak (e.g. a cluster of galaxies) or the sum of two or more less pronounced  $\delta$ -peaks (e.g. groups or filaments aligned along the line of sight...). We shall turn back to this issue later on.

### 3. The data

#### 3.1. Imaging and Photometry

The CFHTLS Deep survey is intimately linked to the Supernovae Legacy Survey (SNLS, Astier et al. (2006)) as they share the same data. In practice, for each observed field data are taken sequentially every 3-4 nights, 6 months per year and in 4 observing bands ( $g'$ ,  $r'$ ,  $i'$ ,  $z'$ ). Additional  $u^*$  data are included but they are not part of the SNLS and do not require time sampling. Most of the data have a seeing requirement limited to  $0.9''$ . Data acquisition is still under progress at CFHT so the depth of the Deep fields is still improving. Data processing (astrometry, photometric calibration, final stacking and production of catalogues) is performed at Terapix<sup>2</sup> for the CFHTLS community. The final data are released regularly by the CADC<sup>3</sup>. The present analysis is based on 2 sets of data released subsequently (the details of the release contents can be found on the Terapix Web site). For the weak lensing signal extraction we used the T0002 data while the deeper images and catalogues from the T0003 release were included for the photometric redshift production.

The Deep survey is made of four independent patches called D1, D2, D3 and D4. For each field and filter, Table 1 summarizes the main observational properties of the T0002 release data in terms of coordinates, seeing, exposure time and depth. Because of the presence of bright stars, fields boundaries, defects in the CCDs and gaps between them with low signal-to-noise ratios, a substantial part of the images cannot be used for weak lensing analysis. Hence, the masked regions generally result in a loss of 20% of the field area. Masks are visible on Fig. 1 where stars have been omitted. The effective usable area is given in Table 1. The total working area for the weak lensing analysis is  $3.61 \text{ deg}^2$ .

#### 3.2. Shear measurement

The coherent stretching of background sources produced by the weak lensing effect is measured using  $i'$  band images. From

<sup>2</sup> <http://terapix.iap.fr/>

<sup>3</sup> <http://cadwww.hia.nrc.ca/>

**Table 1.** Summary of CFHTLS Deep data, release T0002 (July 2005). Limiting magnitudes are expressed in AB system and correspond to 50% completeness.

	D1	D2	D3	D4
$\alpha_{2000}$	02 <sup>h</sup> 25 <sup>m</sup> 59 <sup>s</sup>	10 <sup>h</sup> 00 <sup>m</sup> 28 <sup>s</sup>	14 <sup>h</sup> 19 <sup>m</sup> 27 <sup>s</sup>	22 <sup>h</sup> 15 <sup>m</sup> 31 <sup>s</sup>
$\delta_{2000}$	-04° 29' 40"	+02° 12' 30"	+52° 40' 56"	-17° 43' 56"
$z'$ limit mag	24.9	24.3	24.7	24.9
$i'$	25.9	25.4	25.9	25.7
$r'$	26.1	25.8	26.3	26.3
$g'$	26.3	25.8	26.3	26.3
$u^*$	26.4	26.1	25.8	26.2
$i'$ seeing (")	0.91	0.95	0.91	0.87
Area (deg <sup>2</sup> )	0.93	0.89	0.92	0.86

one field to another the depth of the catalogues is slightly varying but for better coherence between the fields, we define a common magnitude cut for the selection of background sources  $22 < i' < 26$ . In addition, close galaxy pairs with angular separations less than  $3''$  are discarded to avoid blended systems with biased ellipticity measurements. Small galaxies with a half flux radius  $r_h$  smaller than that of stars are also rejected.

The reliability of shear measurements is expected to be comparable to the current cosmic shear survey analyses like the one already performed by Semboloni et al. (2006) in the same fields. Throughout this paper, we report results of shear analysis performed in the  $i'$  band which presents the best balance between depth and seeing. However we checked that we can extract a similar signal in the other noisier  $g'$ ,  $r'$  and  $z'$  bands. This has also been assessed by Semboloni et al. (2006) who report a similar cosmic shear signal in the deep fields using both  $r'$  and  $i'$  bands.

Blurring and distortion of stars and galaxies produced by instrument defects, optical aberration, telescope guiding, atmospheric seeing and differential refraction are corrected using the Point Spread Function (PSF) of stars over the whole field. Several correction techniques and control of systematic errors have been proposed over the past 10 years (see *e.g.* Mellier 1999; Bartelmann & Schneider 2001). In the following we use the most popular KSB method initially proposed by Kaiser et al. (1995). Several teams have already demonstrated that this technique can correct systematics down to a lower value than the very weak cosmic shear signal (van Waerbeke et al. 2005; Heymans et al. 2006). It is therefore well suited for this analysis too. The KSB implementation used here is identical to that of Gavazzi et al. (2004).

The observed ellipticity components  $e_{\alpha=1,2}^{\text{obs}}$  are made of the intrinsic ellipticity components  $e_{\alpha}^{\text{src}}$ , and linear distortion terms that express the instrument and atmospheric contaminations and the contribution of gravitational shear to the galaxy ellipticity. Each ellipticity component is transformed as:

$$e_{\alpha}^{\text{obs}} = e_{\alpha}^{\text{src}} + P_{\alpha\beta}^{\gamma} g_{\beta} + P_{\alpha\beta}^{\text{sm}} q_{\beta}^*, \quad (9a)$$

$$\text{with } P_{\alpha\beta}^{\gamma} = P_{\alpha\beta}^{\text{sh}} - P_{\alpha\gamma}^{\text{sm}} \left( \frac{P^{\text{sh}}}{P^{\text{sm}}} \right)_{\gamma\beta}^*, \quad (9b)$$

where  $g$  is the reduced gravitational shear,  $P^{\text{sm}}$  is the *smear polarisability*,  $P^{\text{sh}}$  the *shear polarisability* and  $P^{\gamma}$  the isotropic circularization contribution to the final smearing. Sources are de-

tected with SExtractor (Bertin & Arnouts 1996) but shape parameters are calculated with Imcat<sup>4</sup>. Because the noise present in these measured quantities is important, all these tensors are simplified to half their trace (see *e.g.* Erben et al. 2001).

$\left( \frac{P^{\text{sh}}}{P^{\text{sm}}} \right)^*$  and  $q^*$  are measured from field stars. Their spatial variation across the field is fitted by a second order polynomial, applied individually to each one of the 36 CCDs composing the MegaCam focal plane. Stars are selected in the magnitude- $r_h$  plane, as usual.  $q^*$  is the anisotropic part of the PSF, which is subtracted from observed ellipticities. The residuals for stars are shown in Fig. 1. After correction, these latter are consistent with a  $\sigma_{\gamma} \simeq 0.004$  rms featureless white noise. In Sect. 4.1, we present mass reconstructions inferred from the shear field measured on distant source galaxies. If we perform the same reconstructions on stars, we only get white noise as expected from a correct PSF smearing correction. Its rms is  $\sigma_{\kappa} \sim 0.001$  when smoothed with a Gaussian kernel of width 1 arcmin, which is much below the signal we are interested in (typically  $0.01 \lesssim \kappa \lesssim 0.5$ , see below).

The smearing part of the PSF contained in the  $P^{\gamma}$  term depends on the magnitude of the object and on its size as compared to the seeing disk. To optimally extract  $P^{\gamma}$ , we derived it from an averaged value over its 40 nearest neighbors in the magnitude- $r_h$  plane. The variance of ellipticities inside this neighborhood is then used as a weighting scheme for the shear analysis. The weight assigned to each galaxy is :

$$w_i = \frac{1}{\sigma_{e,i}^2} = \frac{P^{\gamma 2}}{P^{\gamma 2} \sigma_0^2 + \sigma_i^2}, \quad (10)$$

where  $\sigma_0$  prevents from overweighing some objects. It is set to the 1D intrinsic dispersion in galaxy ellipticities  $\sigma_e = 0.23$  and  $\sigma_i$  is the observed dispersion of ellipticities over the 40 nearest neighbors in the magnitude- $r_h$  plane.

At this level, we have 132,000 (resp. 104,000, 162,000 and 114,000) galaxies with reliable shape parameters in the D1 (resp. D2, D3 and D4) field leading to a source surface number density of  $n_{\text{bg}} = 38.0$  (resp. 30.6, 35.4, 34.5) arcmin<sup>-2</sup>. These value are much higher than usual ones in weak lensing studies, which turn around 15-20 galaxies arcmin<sup>-2</sup>. The magnitude cut  $i' < 26$  explains these high densities although it makes difficult an accurate determination of the redshift distribution of such faint objects. In the following we shall refer to this

<sup>4</sup> <http://www.ifa.hawaii.edu/~kaiser/imcat/>

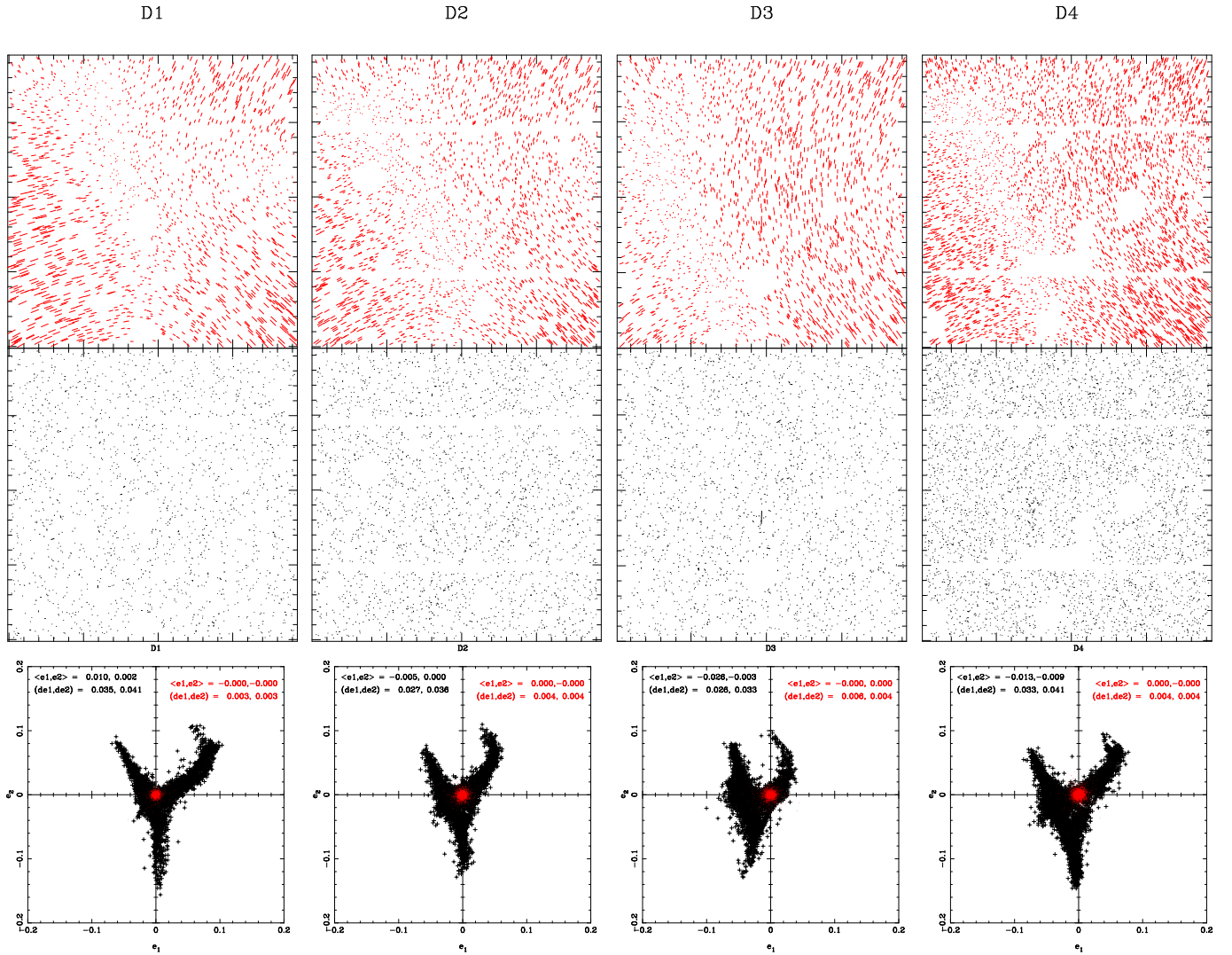


**Fig. 1.** Stellar ellipticities in the CFHTLS Deep fields for D1... D4 from left to right. *Upper row:* polarisation field before and after PSF anisotropy correction (respectively red upper and lower black panels.). *Lower row:* projection of the stellar ellipticities in the  $(e_1, e_2)$  plane before and after PSF anisotropy correction (black crosses and red dots respectively).

source catalogue as CA. Because several galaxies have large uncertainties on their shape parameters, one should correct this density by considering the effective density which would have been achieved if all uncertainties were limited by the intrinsic dispersion in source ellipticity. More precisely if we define  $N_{\text{eff}} = \sum_i (\sigma_e / \sigma_{e,i})^2$ , the effective source number density would then be  $n_{\text{bg}}^{\text{eff}} = 25.3$  (resp. 20.7, 21.6, 21.0)  $\text{arcmin}^{-2}$ . This quantity represents what should be achieved under space-based observing conditions.

### 3.3. Photometric redshifts

The large number of filters available in the CFHTLS Deep images allows a direct estimate of the redshift of each source according to its Spectral Energy Distribution (SED) from  $u^*g'r'i'z'$  bands. The photometric redshifts were measured using the T0003 release catalogues and hyperz<sup>5</sup> software (Bolzonella et al. 2000).

Because we have a bad knowledge of the true redshift distribution of sources in catalogue CA, we consider a subsample that we shall refer to as CB for which reliable  $z_{\text{phot}}$  values are available: good SNR in all  $u^*g'r'i'z'$  bands *i.e.*  $u^* < 28$ ,  $g' < 27.5$ ,  $r' < 27$ ,  $i' < 26$ ,  $z' < 26.5$ , good SED fitting  $\chi^2$  values and  $z_{\text{phot}} \geq 0.11$ . The use of these sub-catalogues prevents a substantial amount of contamination by catastrophic redshifts for nearby sources. Catastrophic redshifts correspond to objects for which  $z_{\text{phot}}$  differs from the true redshift due to degeneracies in the SED shape. They add noise in the redshift distribution which does not correspond to the standard dispersion value  $\sigma_z \sim 0.1$ . This generally occurs at low redshift  $z \lesssim 0.1$  and in the range  $1.4 < z < 2.0$  due to the lack of spectral features in the UV rest-frame or confusion between the Lyman break and the  $4000\text{\AA}$  one. Ilbert et al. (2006) recently studied a comparison between photometric and spectroscopic redshifts in the D1 field observed in the course of the VVDS survey and showed that the quality of CFHTLS Deep data provides valuable photometric redshifts up to  $z \sim 1.4$  for galaxies with  $I_{AB} < 24.0$ .

<sup>5</sup> <http://webast.ast.obs-mip.fr/hyperz/>

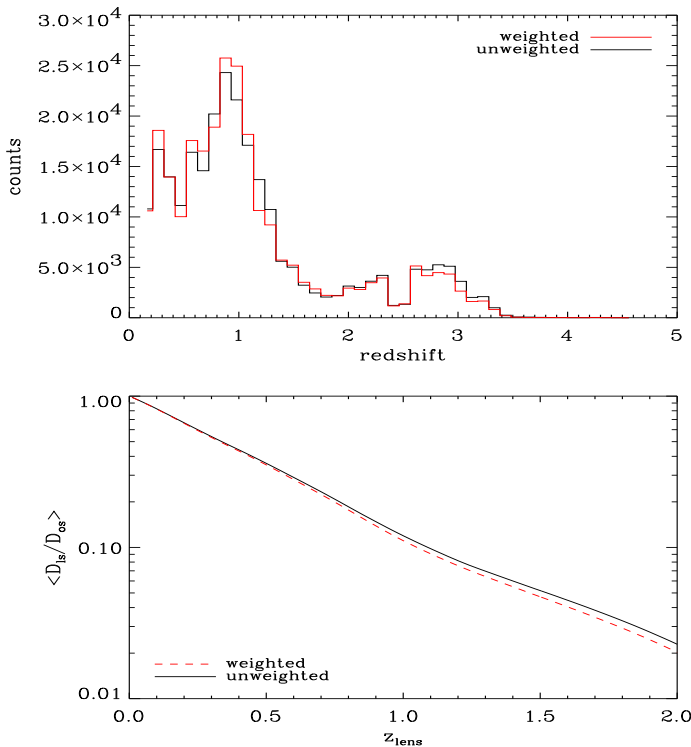


**Fig. 2.** *Upper panel:* Redshift distribution of sources in the sample CB. *Lower panel:* Corresponding average distance factor as a function of the lens redshift. *Solid black:* (resp. *dashed red*) the weighting scheme in Eq. (10) which reduces the contribution of faint-distant sources is (resp. not) taken into account.

The source number density is significantly decreased by this selection. We end up with a number density  $n_{bg} = 21.9, 18.8, 20.6$  and  $17.8 \text{ arcmin}^{-2}$  for D1, D2, D3 and D4 respectively, but we consider that for these catalogues CB, the redshift estimate is reliable within the standard uncertainties of photometric redshifts.

In addition, the weighting scheme we adopted in (10) tends to give less weight to faint sources (which are on average more distant). The weighted redshift distribution of sources in CB is plotted in the upper panel of Fig. 2 and compared to the unweighted distribution. Typically the mean redshift is shifted from 1.15 to 1.11 when accounting for the weighting scheme. Likewise the average distance factor  $W(z_l) = \langle D_{ls}/D_{os} \rangle_{z_s}$  is changed (lower panel of Fig. 2), but except for very distant lenses ( $z \gtrsim 1$ ) the correction is negligible. An empirical fit of  $W(z_l)$  for D1 yields  $W(z_l) \simeq \exp(-z_l/0.55 - z_l^2 + z_l^3/1.2 - z_l^4/5.5)$ ,  $W(z_l)$  being similar for the other fields.

## 4. Mass reconstructions

### 4.1. Convergence maps from observed shear

From the source catalogue CA defined in Sect. 3, we can infer the shear field  $\gamma(\theta)$  and deduce the associated convergence field  $\kappa(\theta)$ . They are related by:

$$\kappa(\theta) = \int_{\mathbb{R}^2} K(\theta - \vartheta) \gamma(\vartheta) d^2\vartheta, \quad (11)$$

where  $K(\theta) = \frac{1}{\pi} \frac{-1}{(\theta_1 - i\theta_2)^2}$  is a complex convolution kernel (Kaiser & Squires 1993) (hereafter KS93). The shear field is smoothed with a Gaussian filter  $G(\theta) \propto \exp(-\frac{\theta^2}{2\theta_s^2})$  with  $\theta_s = 1 \text{ arcmin}$ . The convergence field is consequently smoothed by the same filter. The resulting convergence maps present correlated noise properties (van Waerbeke 2000).

$$\langle \kappa_n(\vartheta) \kappa_n(\vartheta + \theta) \rangle = \frac{\sigma_e^2}{4\pi n_{bg} \theta_s^2} \exp\left(-\frac{\theta^2}{4\theta_s^2}\right). \quad (12)$$

$\sigma_e (4\pi n_{bg} \theta_s^2)^{-1/2}$  characterises the noise level. We measured a value 0.0196, 0.0225, 0.0202 and 0.0221 for D1, D2, D3 and D4, respectively.

In principle, the convergence computed from Eq. (11) must be real and its imaginary component should only be due to noise and possible residual systematics. We checked this assumption by rotating the shear field by  $45^\circ$  and found the reconstructed maps to be consistent with noise as described by Eq. (12).

The KS93 inversion in Eq. (11) is done by a direct summation over all sources without pixelling, smoothing and Fourier transforming the data. This reduces boundary and mask effects on mass reconstructions. Several techniques have been proposed so far since the original KS93 method. Most of them are useful in high shear regions (where  $g \lesssim 1$ ) and for small fields of view. However the wide MegaCam images and the complex field geometry imposed by the masks make difficult, time-consuming and unnecessary the implementation of more complex techniques. In addition, van Waerbeke (2000) has shown that noise properties of KS93 method are well controlled and consistent with Eq. (12).

Fig. 3 shows the convergence maps for D1, D2, D3 and D4 deduced from the catalogue CA. Contours in units of the signal-to-noise ratio (SNR or  $\nu$ ) are overlaid, with  $\nu$  defined as

$$\nu = \text{SNR} = \kappa \frac{(4\pi n_{bg} \theta_s^2)^{1/2}}{\sigma_e}$$

In the present data we detect  $\sim 46$  positive peaks with  $\nu > 3$  and 5 peaks with  $\nu > 4$ . In order to avoid too much contamination by noise peaks but to detect as much true peaks as possible, we therefore fix the threshold at  $\nu = 3.5$ . The 14 peaks detected within this limit will constitute our working sample in the rest of the paper. We discuss in more detail the statistics of these peaks in Sect. 4.2 and their possible association to galaxy clusters in Sect. 5.

### 4.2. Statistics of peaks

Several authors investigated the possibility to use convergence peaks as clusters of galaxies candidates. Simplified analytical calculations based on the Halo Mass Function (as inferred from the Press-Schechter formalism for instance) provided the first predictions for wide field imaging surveys (Schneider 1996; Kruse & Schneider 1999). Then thanks to the development of numerical simulations, quantitative estimates of projection effects and cluster selection functions (in terms of mass and redshift) became available (Reblinsky & Bartelmann 1999; Jain & van Waerbeke 2000; White et al. 2002; Padmanabhan et al.

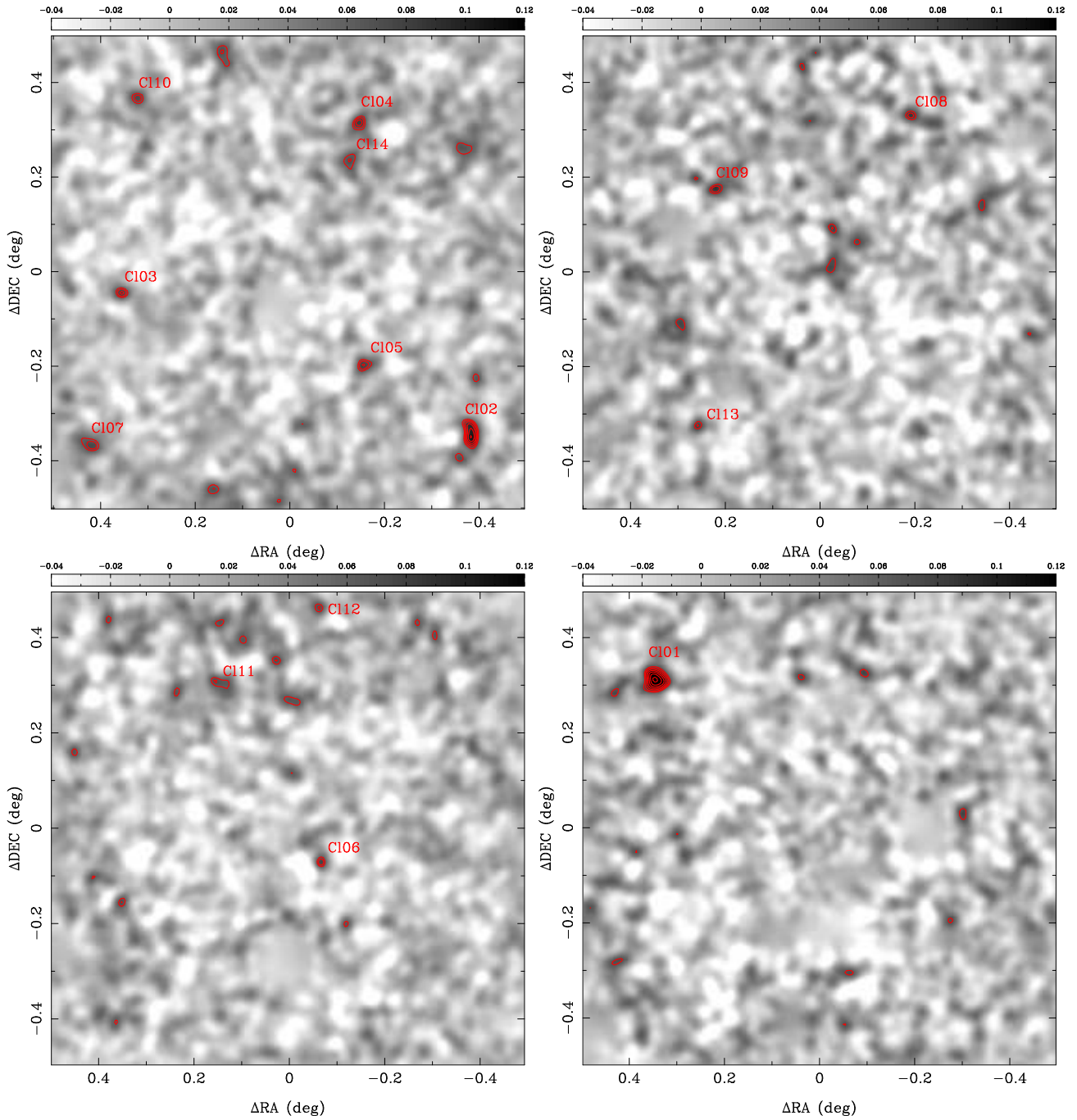


**Fig. 3.** Convergence maps inferred from the ellipticity field of background sources for D1 (top left), D2 (top right), D3 (bottom left) and D4 (bottom right). Contours levels start at  $3\sigma$  with a  $0.5\sigma$  arithmetic increase. The Gaussian filtering scale is 1 arcmin. The 14 peaks with  $\nu > 3.5$  are labeled.

2003; Hamana et al. 2004; Hennawi & Spergel 2005; Tang & Fan 2005).

The practical implementation of a Weak Lensing Cluster Survey (WLCS) requires the control of noise present in observations, either due to the intrinsic ellipticity of sources or to the intervening large scale structures (LSS) along the line of sight. Although the so-called “compensated aperture mass filter” has early been proposed as an efficient filter for peak statistics (Schneider 1996; Kruse & Schneider 1999; Schirmer et al. 2003, 2004; Hettterscheidt et al. 2005), it has been shown

that such a filter may not be as efficient as an optimised filter which would account for the contribution of LSS to the noise budget and the shape of the dark matter halos we aim at detecting (Hennawi & Spergel 2005; Maturi et al. 2005). It turns out that a simple Gaussian filter of width  $\theta_s \sim 1 - 2$  arcmin is close to the optimal linear filter and has been extensively studied in simulations (White et al. 2002; Hamana et al. 2004; Tang & Fan 2005). In addition a promising multiscale wavelets technique has also been proposed recently (Starck et al. 2006) but has not been applied to real data yet. Therefore we shall use

a simple Gaussian filter with scale  $\theta_s = 1$  arcmin as already applied onto the mass reconstructions of Sect. 4.1.

Fig. 4 shows the cumulative number of maxima peaks  $N(> \nu)$  as well as the symmetric number of minima peaks for the four Deep fields. The latter curve is flipped ( $\nu \rightarrow -\nu$ ) for an easier comparison. The net excess of maxima with  $\nu \gtrsim 4$  as compared to minima at the corresponding negative threshold is visible, thus showing the non-Gaussian nature of the convergence field (see also Miyazaki et al. 2002). The statistical significance of this excess is still low due to the large cosmic variance in such a small sky coverage. In addition it should be kept in mind that CFHTLS Deep fields of view were chosen to be free of any massive known nearby cluster.

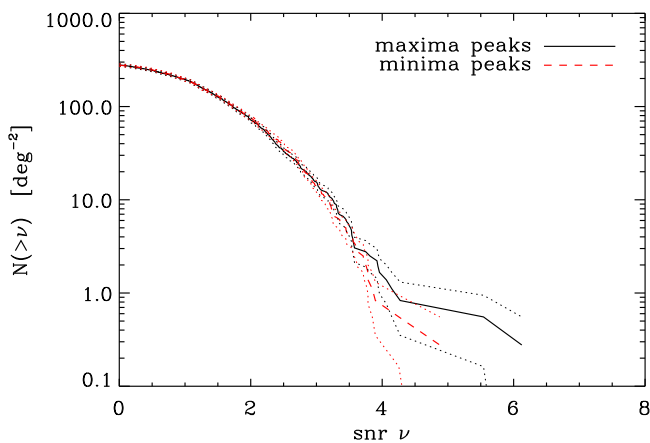


**Fig. 4.** Cumulative counts of  $N(> \nu)$  maxima peaks (solid black) and corresponding counts of  $N(< -\nu)$  minima peaks (dashed blue) curve per square degree in the Deep survey. The surrounding dotted lines represent  $1\sigma$  Poisson errors. The excess of positive maxima is marginally seen as compared to negative minima, thus showing the non-Gaussianity of the convergence field.

An extensive study of  $\kappa$ -peaks statistics in the Wide CFHTLS survey would provide valuable cosmological information for cosmic shear studies and would help breaking some degeneracies (mainly between  $\Omega_m$  and  $\sigma_8$ ) present in the shear 2-point correlation function. Such an analysis is beyond the scope of the present work but the full implementation of the  $\kappa$ -peaks statistics in the presently released CFHTLS-Wide data is in progress. It is noteworthy that in order to extract the associated cosmological signal, there is no need to measure the mass or the redshift of the peaks, neither to identify them with clusters (or projected groups, etc...). This is a real advantage of the method compared to cluster physics driven by optical, X-ray or SZ surveys.

However, instead of a blind study of the convergence peaks, we propose in the following to fully characterise the structures responsible for the highest convergence maxima peaks. We also wish to analyse what are they made of, in terms of dark matter and galaxies contents or false detections.

### 4.3. Convergence maps expected from light

In order to check the global agreement between the weak lensing mass reconstructions and the distribution of foreground galaxies, we create fiducial convergence maps from the spatial distribution of early-type galaxies since we know that they are fair tracers of the density contrast (e.g. Kaiser et al. 1998; Gray et al. 2002; Gavazzi et al. 2004).

The availability of photometric redshifts makes possible the identification of such massive galaxies as a function of lens redshift since the photometric redshift code hyperz also provides spectral types. We consider in the following a simple relation between mass and galaxy densities. We restrict ourselves to bright elliptical galaxies with  $i' \leq 23$ , well below the detection limit  $i' \sim 26$ . We assume that all the mass in excess of the background density is in the form of haloes around massive E/SO galaxies with a truncated isothermal density profile of the three-dimensional and projected forms

$$\begin{aligned} \rho(r) &= \frac{M}{2\pi^2} \frac{r_t}{r^2(r_t^2 + r^2)} \\ \Sigma(R) &= \frac{M}{2\pi r_t} \left[ R^{-1} - (R^2 + r_t^2)^{-1/2} \right] \end{aligned} \quad (13)$$

respectively. We further assume a truncation radius  $r_t$  which scales as  $r_t/r_{t*} = (L/L_*)^{1/4}$  with  $r_{t*} = 264$  kpc to roughly mimic the results obtained by Gavazzi et al. (2004) and Hoekstra et al. (2004). The scaling relation between mass and luminosity is of the form  $M/M_* = (L/L_*)^\beta$ . We use a typical mass  $M_* = 2 \times 10^{12} h_{70}^{-1} M_\odot$  with a luminosity  $L_* = 2.2 \times 10^{10} h_{70}^{-2} L_\odot$  in the rest-frame  $r'$  band.  $\beta$  is left as a free parameter which we vary from 0 (constant mass) to 1 (constant M/L). The very details of the halo density profile used in this analysis is not relevant for the purpose of comparing dark matter and galaxy distributions at intermediate to large scales. However, although this issue will not be addressed here, it is worth mentioning that such comparison, *i.e.* the so-called galaxy-galaxy lensing, provides insightful constraints on the density profile of halos (e.g. Hoekstra et al. 2004; Mandelbaum et al. 2005; Hoekstra et al. 2005). Here we assume an input realistic halo density profile to infer a convergence-from-light distribution  $\kappa_l$ .

Hence, the sample of  $N_{\text{lens}}$  lenses at redshift  $z_i$ , proper distance  $l_i$ , angular distance  $D_{oi}$ , angular position  $\theta_i$  and luminosity  $L_i$  allows to write the matter density in excess at proper distance  $l$  and angular position  $\theta$  in the form

$$\rho(l, \theta) - \bar{\rho} = \sum_{i=1}^{N_{\text{lens}}} \delta_D(l - l_i) \Sigma_* [D_{oi}(\theta - \theta_i)] \left( \frac{L_i}{L_*} \right)^\beta, \quad (14)$$

where  $\delta_D$  is the Dirac distribution and  $\Sigma_*$  is the surface density for a characteristic halo of luminosity  $L_*$ . Since we do not know the exact redshift distribution of sources in sample CA which is required to calculate  $W(z_i)$  in Eq. (8), we use the empirical redshift distribution found for the source sample CB in Sect. 3.3. In addition, since we cannot consider the lens sample as flux-limited, due to the complex cuts in magnitude and  $z_{\text{phot}}$  SED fitting  $\chi^2$  values (which depend on colour, spectral type, magnitude...), it is difficult to estimate its completeness. Therefore, we restrict ourselves to a qualitative comparison between convergence maps inferred from shear and from light.

We insert Eq. (14) into Eq. (8) to derive the associated  $\kappa_l$  map, smooth it with the same Gaussian filter as the one applied onto the noisy data in the previous section and compare the  $\kappa_l$ -maps to the shear-inferred  $\kappa$ -maps. For each field D1, D2, D3 and D4, we consider two cases  $\beta = 1$  (mass scales like luminosity) in Fig. 5 and  $\beta = 0$  (every galaxy has the same mass) in Fig. 6. Although a quantitative analysis is not possible due to incompleteness and the fact that CA and CB sources samples have different redshift distributions, the qualitative global agreement between maps is convincing, especially in D1 and D4 fields which contain the most prominent peaks.

Only few low significance  $\kappa$ -peaks ( $\nu \leq 3.5$ ) are associated with  $\kappa_l$  overdensities whereas most ( $\nu \geq 4$ )  $\kappa$ -peaks match a  $\kappa_l$  bright peak. A detailed comparison is done in Sect. 5.

## 5. Properties of $\nu > 3.5$ peaks

In this section we attempt to estimate the redshift, mass and luminosity of structure(s) responsible of the 14  $\kappa$ -peaks with  $\nu \geq 3.5$ . This significance threshold is rather low so we expect a substantial amount of contamination by noise fluctuations. However the purpose, here, is not to use the statistics of peaks (free from false detections) as a cosmological probe. Instead we are more interested in the intrinsic properties of the detected peaks and whether they appear close to galaxies overdensities *i.e.* they are likely due to clusters. So the first step in this peak identification is to estimate a redshift, taking advantage of the availability of photometric redshifts. Two methods are explored, one which is directly related to the shear signal dependency on lens redshift and which does not require an explicit identification of the peak with galaxies, and the other which is related to the photometric redshift distribution of an overdensity of galaxies associated with the mass peak. Results from the two approaches are summarised in Table 2.

### 5.1. Lens tomography

The basic principle of the lens tomography and its lens redshift estimate, introduced and already applied by Wittman et al. (2001, 2003) and Hennawi & Spergel (2005), is the following: in the case of a real shear peak at redshift  $z_l$ , the source redshift dependency of the shear signal must follow a characteristic law according to  $w(z_l, z_s) = D_{ls}/D_{os}$ . The shape of the shear strengthening versus the source redshift allows to infer the lens redshift. In the following, we apply this technique to estimate the lens redshift of each peak and check whether the shear behavior around peaks is consistent with lensing or is rather a noise fluctuation.

We measure each shear profile between 1 and 5 arcminutes from the peak centre, using the source catalogue CB for which photometric redshifts are available. Assuming that the lens mass distribution at redshift  $z_l$  follows a Singular Isothermal Sphere (SIS) profile, the shear is simply

$$\gamma(\theta, z_s) = w(z_l, z_s) \frac{\theta_E}{2\theta}. \quad (15)$$

The Einstein radius  $\theta_E$  is related to the characteristic cluster velocity dispersion by  $\sigma_v = 186.2 \text{ km s}^{-1} (\theta_E/1'')^{1/2}$ . We fit the

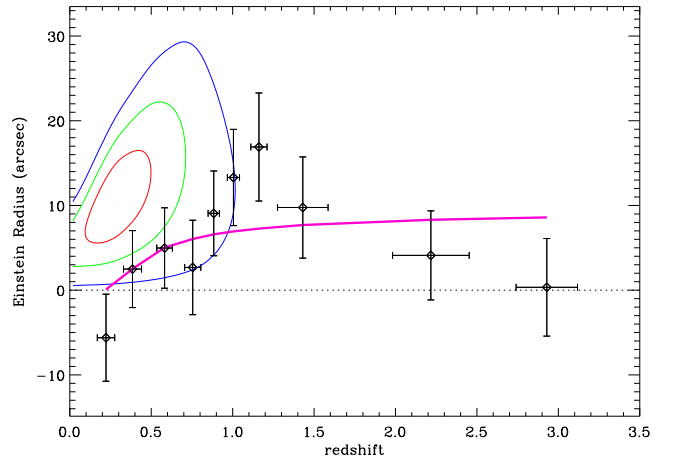


**Fig. 7.** Increase of shear signal strength (*i.e.* equivalent Einstein radius) as a function of source redshift in the CB source catalogue split into 10 quantiles around peak CI-02. This allows to fit for the lens redshift  $z_l$  and Einstein radius  $\theta_E$  simultaneously. Contours show 1, 2 and 3  $\sigma$  CL regions around the best fit  $\theta_E$  and  $z_l$ . Peak CI-02 exhibits the expected profile for a cluster with velocity dispersion  $\sigma_v = 600 \pm 100 \text{ km s}^{-1}$  and redshift  $z_l = 0.28 \pm 0.10$  with  $\chi^2/\text{dof} = 0.8$  (thick line).

shear function for the unknown lens redshift  $z_l$  and Einstein radius  $\theta_E$  by minimising a  $\chi^2(z_l, \theta_E)$  of the form

$$\chi^2(z_l, \theta_E) = \sum_i \frac{(e_{t,i} - w_i \frac{\theta_E}{2\theta_i})^2}{\sigma_{e,i}^2} \quad (16)$$

where  $w_i = w(z_l, z_{s,i})$ ,  $\sigma_{e,i}$  is given by Eq. (10) and  $e_{t,i}$  is the tangential component of ellipticity. The dependency of  $\chi^2$  with  $\theta_E$  can be easily removed by considering that  $\frac{\partial \chi^2}{\partial \theta_E} = 0$  for any  $z_l$  so that the trivial solution

$$\hat{\theta}_E = \frac{2 \sum_i \frac{e_{t,i} w_i}{\theta_i \sigma_{e,i}^2}}{\sum_i \frac{w_i^2}{\theta_i^2 \sigma_{e,i}^2}} \quad (17)$$

can be inserted into Eq. (16) to give

$$\chi^2(z_l) = \sum_i \frac{e_{t,i}^2}{\sigma_{e,i}^2} - \frac{\left( \sum_i \frac{e_{t,i} w_i}{\theta_i \sigma_{e,i}^2} \right)^2}{\sum_i \frac{w_i^2}{\theta_i^2 \sigma_{e,i}^2}}. \quad (18)$$

In order to illustrate the method we plot on Fig. 7 the value of the Einstein radius measured in the 10  $z_s$  quantiles of sources between 1 and 5 arcmin from the centre of the peak CI-02, detected with  $\nu = 5.5$ . The increase of  $\theta_E$  with redshift  $z_s$  is clear and allows an unambiguous identification of the lens redshift. Contours show the 68.3%, 95.4% and 99.3% CL regions for  $z_l$  and  $\theta_E$ . The thick curve represents the function  $\theta_E \times w(z_l, z_s)$  for the best fit values  $z_l = 0.28 \pm 0.10$  and  $\theta_E = 10 \pm 3''$  leading to a velocity dispersion  $\sigma_v = 600 \pm 100 \text{ km s}^{-1}$ . Because of the rather large statistical uncertainties, the detailed radial shape of the shear profile introduced in the  $\chi^2$  fit is not much important. However for significant peaks in the reconstructed mass maps a redshift estimate directly evaluated from the lensing properties

**Fig. 5.** Convergence maps inferred from the distribution of Early-type lens galaxies assuming that  $M_{\text{halo}} \propto L$  (exponent  $\beta = 1$  in (14)) for D1 (top left), D2 (top right), D3 (bottom left) and D4 (bottom right). The Gaussian filtering scale is 1 arcmin. The red contours of the convergence maps inferred from the observed shear are overlaid for comparison with Fig. 3. Masked regions are set to zero convergence value.

**Fig. 6.** Same as Fig. 5 with exponent  $\beta = 0$ , *i.e.* all lens galaxies have the same halo mass.

of the peaks is a viable method. It could in particular be applied to any “dark clump” where no bright galaxies can be associated with the mass peaks.

Using lensing tomography for the whole catalogue CB and the whole Deep fields, it is possible to put constraints on the lens redshift for 8 peaks as shown in Table 2. If the signal-to-noise ratio is too low or  $\chi^2/\text{dof} > 2$ , the inferred lens redshift is systematically set to  $z_l = 0$ .

We also note in Table 2 that peaks exhibit fitted velocity dispersion values limited to  $\sigma_v \lesssim 600 \text{ km s}^{-1}$ . There is no massive cluster with  $\sigma_v > 800 \text{ km s}^{-1}$  below redshift  $\sim 0.7$  in the Deep survey. This is not a surprise as the Deep fields were initially selected for their lack of well identified Abell clusters for example.

## 5.2. Optical counterparts

In this section we take advantage of the deep multiband photometry of the CFHTLS data to check whether an optical counterpart can be assigned to our 14 high convergence peaks with  $\nu > 3.5$ .

We first examine galaxies in a circular aperture of 4 arcmin around each peak. This radius corresponds to a linear scale of 200 to 400 kpc for a lens redshift ranging from 0.2 to 0.7 respectively and is representative of typical core radius values for rich clusters. Therefore this is the radius within which the most significant density of bright galaxies is expected, most of them being early-type galaxies. We then require that an excess of galaxies is present and well localised in the photometric redshift distribution once the background  $z_{\text{phot}}$  distribution is subtracted. The background is defined in the region beyond 6 arcmin of *all peaks*. If a red cluster sequence (RCS) is found in the ( $i'$ ,  $r' - i'$ ) colour–magnitude diagram by a visual inspection (see Fig. 8), we also check that the  $z_{\text{phot}}$ -distribution of the bright RCS members (*i.e.* having  $i' < 22$ ) lie at the same redshift as the whole galaxy excess.

8 peaks out of 14 meet these criteria whereas there is no clear optical associable counterpart for the remaining 6 peaks. For each of the former 8  $\kappa$ -peaks, we define the cluster redshift as the location of the most prominent  $z_{\text{phot}}$  excess peak in the  $z_{\text{phot}}$  averaged histogram. The error on the redshift is found by fitting the excess as a Gaussian distribution. We also define the luminosity-weighted optical centre using the bright galaxies ( $i' < 22$ ) in the  $z_{\text{phot}}$  excess range. Optical centres are less than one arcmin away from the convergence peak location, as expected from the spatial resolution of the mass maps. The observed offsets are reported in Table 2 in column  $\Delta(\alpha, \delta)$ .

In order to characterise the galaxy content around  $\kappa$ -peaks we also estimate the distribution of  $i'$  magnitudes in a fiducial projected radius  $R = 1 \text{ Mpc}$  in excess of the background distri-

bution and corrected for the lack of information in the masked regions. The resulting distribution is fitted by a Schechter luminosity function of the form

$$\phi(m) = \eta \phi_* 10^{0.4(1+\alpha)(m_* - m)} \exp(-10^{0.4(m_* - m)}) \quad (19)$$

with a fixed slope  $\alpha = -1$  and  $\eta = 0.4 \ln 10 = 0.921$ .  $m_*$  and  $\phi_*$  are left free. The value of the slope is consistent with that derived from the  $r'$  rest frame luminosity function of the local Universe measured from the SDSS data (Blanton et al. 2003). We then define the richness  $\Lambda = \phi_* \Gamma(2 + \alpha)$  as the equivalent number of galaxies with characteristic magnitude  $m_*$  in the projected radius  $R = 1 \text{ Mpc}$ . For each field, we estimate and subtract the background in the complementary area after excluding circles of radius 1.5 Mpc around all peaks. Richness is reported in Table 2. Two examples of magnitude excess are given in the bottom panels of Fig. 8.

At this level it is worth mentioning that Cl-02 has a large but broad excess of galaxies in the redshift distribution spanning between  $z = 0.3$  and  $z = 0.8$ . It is not possible to isolate a well defined RCS (upper right panel of Fig. 8). Cl-02 is likely a projection effect due to the alignment of several structures along the line of sight. This illustrates the importance of projection effects, even for highly significant detections since Cl-02 has a SNR  $\nu = 5.5$ . Therefore the richness of Cl-02 cannot be inferred from the data. This is clearly seen in the lower right panel of Fig. 8 where the excess magnitude distribution is not consistent with a Schechter luminosity function. Further studies on Cl-02 would require spectroscopic information in order to disentangle the various contributions to shear signal at different redshifts.

We note that the optical counterpart of Cl-14 is also difficult to characterise. Although it exhibits a clear RCS at redshift  $z \sim 0.17$  consistent with the XMM/LSS detection (see next section), the luminosity function is not well fit by a Schechter function and suggests an additional structure at higher redshift ( $z \sim 0.3 - 0.5$ ).

From the new defined centre and photometric cluster redshift, we re-estimate the lensing velocity dispersion from the catalogue CB of background sources. In Table 2, we report the new values of the lensing velocity dispersion. They do not change significantly as these global measurements (total mass, velocity dispersion, ...) only weakly depend on the precise location of the center.

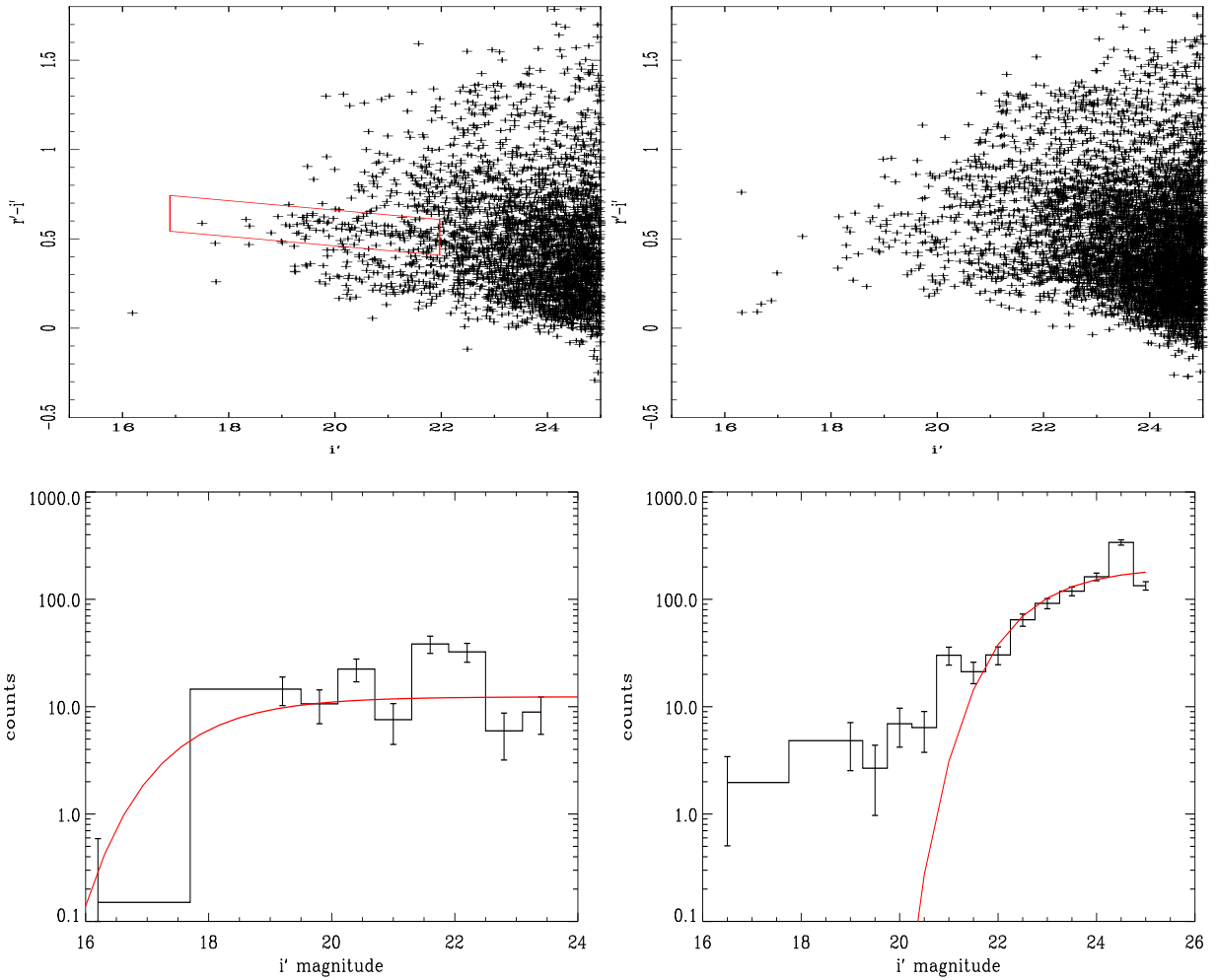


**Fig. 8.** *Upper panels:*  $(i', r' - i')$  colour-magnitude diagram for Cl-07 exhibiting a clear RCS (left) and Cl-02 with no RCS (right). *Lower panels:*  $i'$  band magnitude excess (*i.e.* luminosity function) for the same Cl-07 and Cl-02 peaks (respectively left and right panels). The former has a distribution which is consistent with a Schechter function whereas the latter has not, thus suggesting that Cl-02 is made of several projected structures along the line of sight (see text).

### 5.3. Comparison to X-ray data

The CFHTLS-Deep D1 field is part of the XMM/LSS survey<sup>6</sup>. We therefore took advantage of the publicly available X-ray database to cross-correlate our sample of  $\kappa$ -peaks/clusters with those X-ray detections published in (Valtchanov et al. 2004; Willis et al. 2005; Pierre et al. 2006).

The matching is very good. More precisely, over the seven  $\nu > 3.5$  peaks detected in D1, four are XMM-LSS clusters with luminosity  $1.5 \cdot 10^{43} \leq L_{X,\text{bol}} \leq 6.5 \cdot 10^{43}$  erg/s and temperature  $1 \lesssim T_X \lesssim 2$  keV. However, the most pronounced  $\nu = 5.5$  D1 peak, namely Cl-02, is not part of the XMM/LSS sample. This is consistent with the evidence we highlighted above that this peak corresponds to a projection of several less massive clusters/groups along the line of sight. X-ray detections would not be as sensitive as optical/lensing detections since X-ray emissivity is the integral of the squared electron density along

the line of sight whereas optical/lensing signal scales like the galaxy/total matter density respectively, so projection effects should be much less frequent in X-ray samples.

Concerning the peaks Cl-03 and Cl-10, which do not exhibit any optical counterpart, there is no X-ray detections. Therefore, as already pointed out, this confirms that Cl-03 and Cl-10 are likely false detections due to noise fluctuations.

There are 9 publicly available XMM/LSS clusters in the D1 field of view. 4 of them are part of our weak lensing cluster sample although we note that a  $\nu = 3.4$  peak at  $\alpha = 02^{\text{h}} 24^{\text{m}} 31.7^{\text{s}}$  and  $\delta = -04^{\circ} 13' 55''$  is also part of the XMM/LSS sample (XLSSC44 at  $z = 0.26$ ,  $T_X = 1.37^{+0.28}_{-0.16}$  keV). This cluster has been missed by the weak lensing survey because it does not meet the  $\nu > 3.5$  detection threshold. The remaining 4 XMM/LSS clusters which are not part of our sample: XLSSC38 ( $z = 0.58$ ,  $T_X$  unknown), XLSSC11 ( $z = 0.05$ ,  $T_X = 0.64^{+0.11}_{-0.07}$  keV), XLSSC29 ( $z = 1.05$ ,  $T_X = 4.07^{+1.72}_{-0.99}$  keV) and XLSSC5 ( $z = 1.05$ ,  $T_X = 3.67^{+3.50}_{-1.33}$  keV) are either very low or very high redshift clusters for which lensing efficiency

<sup>6</sup> [http://vela.astro.ulg.ac.be/themes/spatial/xmm/LSS/index\\_e.html](http://vela.astro.ulg.ac.be/themes/spatial/xmm/LSS/index_e.html), see also <http://13sdb.in2p3.fr:8080/13sdb/>

is low. Therefore it is not surprising that they are missing in our weak lensing sample.

Note also that the peak CI-01, located in D4 and which is the strongest peak matches an X-ray detected ROSAT cluster at redshift  $z = 0.13$  and luminosity  $L_{X,[0.5-2.0]} = 14.5 \pm 2.5 \times 10^{43}$  erg/s (de Grandi et al. 1999).

## 6. Discussion

### 6.1. Global statistics

The statistics of peaks over the four CFHTLS Deep fields suggest several comments.

Our cluster candidates are not very massive systems but look more like small clusters / large groups having  $\sigma_v \sim 500 \text{ km s}^{-1}$ . The lack of massive clusters is not surprising since the Deep field of view is only  $4 \text{ deg}^2$  and the 4 MegaCam fields were selected *a priori* as free from already known rich clusters. It turns out that half of the  $\nu > 3.5$  convergence peaks (either with or without an optical counterpart) are in D1 and at redshift  $z \sim 0.28$ , *i.e.* in the redshift range with best lensing efficiency. How much of this excess is due to the 10% lower noise level in D1 relative to D2, D3, D4 or is pure sample variance (enhanced by the strong spatial clustering of galaxy clusters)? The latter is our favoured explanation since a 10% change in SNR for D1 peaks would not significantly change the ranking of peaks in Table 2. At  $z \sim 0.28$ , 1 deg scale corresponds to  $15h_{70}^{-1} \text{ Mpc}$  and the cosmic variance of the cluster-cluster correlation function is still important. Moreover thanks to image depth, the large number density of background sources allows to detect clusters with a velocity dispersion as low as  $\sigma_v \sim 500 \text{ km s}^{-1}$ . Weak lensing-based clusters surveys (WLCSs) will be fully efficient in much wider fields of view hosting several massive clusters. Translating the detections we got in the Deep fields into predictions for the CFHTLS Wide survey suggests that a detection threshold as high as  $\nu \gtrsim 4.5$  will be required for secure WLCSs since the noise level due to random source ellipticities in this shallower survey will be much larger. This will be done at the expense of finding intermediate mass structures with  $\sigma_v \sim 400 - 700 \text{ km s}^{-1}$ , which will be investigated with alternative strong lensing methods (Cabanac et al. 2006)<sup>7</sup>.

We found that  $\sim 50\%$  of our  $\nu > 3.5$  candidates turn out to be false or inconclusive detections. All the D1 XMM/LSS clusters that lie in the lensing relevant redshift range  $0.1 \lesssim z \lesssim 0.5$  are detected with a SNR  $\nu \gtrsim 3.4$ . This redshift range is therefore devoid of any massive cluster. An important outcome of this analysis is the confirmation that projection effects may be severe for WLCS purposes. CI-02 which is a  $\nu = 5.5$  convergence peak shows up due the contribution of several structures at different redshifts thus mimicking the effect of a single massive cluster. The optical counterpart of CI-14 is also unclear although it would be natural to associate it with XLSSC41 at  $z = 0.17$ . Except CI-02, none of our secure D1  $\kappa$ -peaks with an optical counterpart are unobserved with X-rays. Therefore the completeness of WLCSs is lower than X-ray techniques for clusters detections. If one aims at reducing the amount of

false detections (higher efficiency), the sample completeness of WLCSs turns out to be very low. This has already been pointed out in simulations (*e.g.* White et al. 2002; Hamana et al. 2004; Hennawi & Spergel 2005).

The theoretical analysis of Hamana et al. (2004) is well suited for a direct comparison with our results since the survey area, the smoothing scale, and the noise properties are the same. We found a satisfying agreement when considering their Fig. 7 although the sample variance is large.

### 6.2. Physical properties of clusters

The Deep survey sky coverage is not wide enough for further cosmological interpretation of these results. Nevertheless it is interesting to study the physical properties of our shear-selected cluster sample. Are weak lensing detections biased toward peculiar systems? Such a sample is suitable for the necessary calibration of other cluster detection methods, especially for cosmological purposes.

A direct comparison between lensing velocity dispersion and richness is shown in the upper panel of Fig. 9 for the six systems CI-01, CI-03, CI-05, CI-07, CI-08 and CI-12 for which a clear optical counterpart and measurable richness are found. The range of richness and velocity dispersion probed by our sample is quite narrow although a direct linear regression yields a best fit scaling relation  $\sigma_v \sim 258 \text{ km s}^{-1} \Lambda^{0.17}$ . However a linear fit of the form  $\sigma_v \sim 81 \text{ km s}^{-1} \Lambda^{0.5}$  (with a slope consistent with virial equilibrium) also provides a good fit to the data. As far as we know there is no published comparison between richness and lensing velocity dispersion in the literature. It is therefore impossible to extend this study either toward massive clusters or toward groups of galaxies to put tighter constraints on this scaling relation. A detailed comparison between richness and weak lensing signal is left for a future work (see also Olsen et al. 2006).

In the lower panel of Fig. 9 we also compare lensing velocity dispersion and X-ray temperature for the five D1 XMM/LSS clusters CI-03, CI-05, CI-07, CI-14 and XLSSC44. More precisely and following Cypriano et al. (2004), we compare the lensing velocity dispersion inferred temperature  $k_B T_{\text{lens}} = \mu m_H \sigma_v^2$  of dark matter particles to the X-ray temperature of hot ICM gas particles.  $\mu m_H$  is the mean nucleon mass per free electron. For comparison we take the same  $\mu = 0.61$  value as Cypriano et al. (2004). We also include in the comparison data from the study of Bardeau et al. (2006) of 11 X-ray luminous clusters at  $z = 0.2$ . Under the assumption of energy equipartition these temperatures would be equal. If non gravitational sources of gas heating/cooling are at work we expect some departures from this relation  $T_X \neq T_{\text{lens}}$ . Conversely the mass (and thus  $\sigma_v$  and  $T_{\text{lens}}$ ) of shear-selected clusters may be increased by projections of unrelated material along the line of sight.

Although the statistics is poor for massive clusters ( $T_X \gtrsim 3 \text{ keV}$ ), the lower panel of Fig. 9 suggests that shear-selected clusters are well aligned onto the bisectrix  $T_X = T_{\text{lens}}$ . In other word, gas and collisionless particles share the same amount of energy. This behaviour seems to be less true for massive clusters. For example Cypriano et al. (2004) found that for  $T_X \gtrsim 8$

<sup>7</sup> See also <http://www.cfht.hawaii.edu/~cabanac/SL2S/>

**Table 2.** Catalogue of convergence peaks / galaxy clusters in CFHTLS Deep fields.

ID	Convergence peak					Optical counterpart					X-ray counterpart	
	$\alpha$ J2000	$\delta$ J2000	$\nu$	$\sigma_{v,lens}$ $\text{km s}^{-1}$	$z_{\text{tomo}}$	$\Delta(\alpha, \delta)$ arcsec	$z_{\text{phot}}$	$\sigma_{v,lens}$ $\text{km s}^{-1}$	$\Lambda$	RCS	$L_{X,[0.5-2.0]}$ $10^{43}$ erg/s	$T_X$ keV
CI-01	22 <sup>h</sup> 16 <sup>m</sup> 58 <sup>s</sup>	-17° 25' 10"	6.2	612 <sup>+102</sup> <sub>-73</sub>	0.05 ± 0.12	(-15,-16)	0.15 ± 0.04	618 <sup>+89</sup> <sub>-106</sub>	40 <sup>+8</sup> <sub>-6</sub>	Y	14.5 ± 0.2 <sup>a</sup>	
CI-02	02 <sup>h</sup> 24 <sup>m</sup> 27 <sup>s</sup>	-04° 50' 34"	5.5	604 <sup>+98</sup> <sub>-115</sub>	0.27 ± 0.13	(12,17)	0.39 ± 0.22	648 <sup>+191</sup> <sub>-284</sub>	?	?	X	X
CI-03	02 <sup>h</sup> 27 <sup>m</sup> 24 <sup>s</sup>	-04° 32' 19"	4.1	539 <sup>+142</sup> <sub>-135</sub>	0.36 ± 0.20	(2,1)	0.26 ± 0.03	516 <sup>+125</sup> <sub>-166</sub>	57 <sup>+12</sup> <sub>-10</sub>	Y	~ 1.5 <sup>b</sup>	1.02 <sup>+0.19</sup> <sub>-0.15</sub>
CI-04	02 <sup>h</sup> 25 <sup>m</sup> 24 <sup>s</sup>	-04° 10' 48"	4.1	587 <sup>+129</sup> <sub>-117</sub>	0.32 ± 0.17	-	-	-	-	N	X	X
CI-05	02 <sup>h</sup> 25 <sup>m</sup> 21 <sup>s</sup>	-04° 41' 33"	4.0	505 ± 95	0.21 ± 0.12	(10,18)	0.23 ± 0.03	427 <sup>+132</sup> <sub>-196</sub>	19 <sup>+4</sup> <sub>-3</sub>	Y	~ 5.2 <sup>c</sup>	2.02 <sup>+0.49</sup> <sub>-0.28</sub>
CI-06	14 <sup>h</sup> 19 <sup>m</sup> 01 <sup>s</sup>	+52° 36' 43"	3.8	440 ± 65	0.00 ± 0.10	-	-	-	-	N		
CI-07	02 <sup>h</sup> 27 <sup>m</sup> 40 <sup>s</sup>	-04° 51' 38"	3.8	474 <sup>+83</sup> <sub>-69</sub>	0.00 ± 0.18	(-25,12)	0.25 ± 0.09	517 <sup>+133</sup> <sub>-186</sub>	37 <sup>+10</sup> <sub>-7</sub>	Y	~ 6.5 <sup>d</sup>	1.71 <sup>+0.15</sup> <sub>-0.11</sub>
CI-08	10 <sup>h</sup> 01 <sup>m</sup> 21 <sup>s</sup>	+02° 22' 58"	3.7	392 ± 91	0.06 ± 0.21	(-10,-43)	0.62 ± 0.05	347 <sup>+272</sup> <sub>-347</sub>	43 <sup>+8</sup> <sub>-6</sub>	Y		
CI-09	09 <sup>h</sup> 59 <sup>m</sup> 42 <sup>s</sup>	+02° 32' 20"	3.7	552 <sup>+208</sup> <sub>-113</sub>	0.26 <sup>+0.39</sup> <sub>-0.16</sub>	-	-	-	-	N		
CI-10	02 <sup>h</sup> 27 <sup>m</sup> 16 <sup>s</sup>	-04° 07' 37"	3.7	380 ± 63	0.00 ± 0.18	-	-	-	-	N	X	X
CI-11	14 <sup>h</sup> 20 <sup>m</sup> 28 <sup>s</sup>	+52° 59' 22"	3.6	311 <sup>+283</sup> <sub>-376</sub>	0.00 ± 1.00	-	-	-	-	N		
CI-12	14 <sup>h</sup> 19 <sup>m</sup> 02 <sup>s</sup>	+53° 08' 44"	3.6	353 <sup>+211</sup> <sub>-99</sub>	0.00 ± 0.21	(49,-17)	0.24 ± 0.04	334 <sup>+183</sup> <sub>-334</sub>	68 <sup>+9</sup> <sub>-8</sub>	N		
CI-13	10 <sup>h</sup> 01 <sup>m</sup> 30 <sup>s</sup>	+01° 53' 04"	3.6	536 ± 60	0.00 ± 0.09	-	-	-	-	N		
CI-14	02 <sup>h</sup> 25 <sup>m</sup> 29 <sup>s</sup>	-04° 15' 34"	3.6	492 ± 164	0.34 ± 0.16	(-12,28)	0.17 ± 0.07	481 <sup>+150</sup> <sub>-245</sub>	?	Y	~ 2.4 <sup>e</sup>	1.34 <sup>+0.21</sup> <sub>-0.10</sub>

(a) ROSAT cluster (22<sup>h</sup> 16<sup>m</sup> 56.2<sup>s</sup>, -17° 25' 25.5") at  $z = 0.13$  (de Grandi et al. 1999),

(b) XMM/LSS cluster at  $z = 0.31$  (XLSSC13),

(c) XMM/LSS cluster at  $z = 0.26$  (XLSSC25),

(d) XMM/LSS cluster at  $z = 0.29$  (XLSSC22),

(e) XMM/LSS cluster at  $z = 0.14$  (XLSSC41).

All XMM/LSS data (b,c,d,e) are from (Willis et al. 2005; Pierre et al. 2006).

In columns RCS, the flag is set Y if a Red Clusters Sequence is found by a simple visual inspection. Otherwise it is N.

Rows filled with "?" correspond to peaks with an optical counterpart for which the richness is meaningless (projection of several structures along the line of sight). Rows filled with "-" are likely false detections without a reliable optical counterpart. Rows filled with "X" are in the D1 field part of the XMM/LSS survey but not detected in X-rays.

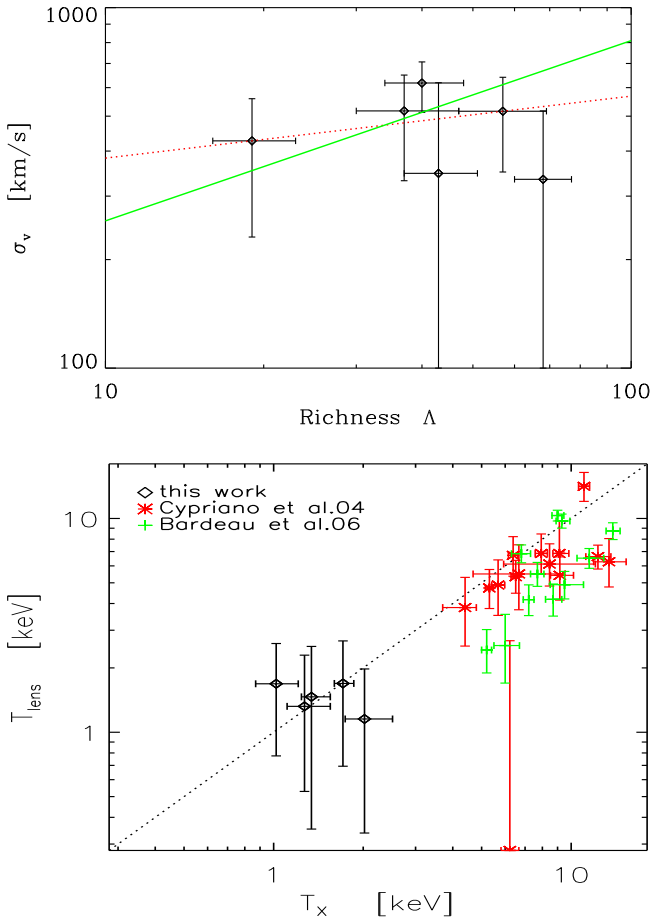


**Fig. 9.** *Upper panel:* Correlation between richness and lensing velocity dispersion for CI-01, CI-03, CI-05, CI-07, CI-08 and CI-12. The dotted red line is a raw linear fit leading to the scaling  $\sigma_v \sim 258 \text{ km s}^{-1} \Lambda^{0.17}$  whereas the solid green curve assumes a virial-like slope yielding  $\sigma_v \sim 81 \text{ km s}^{-1} \Lambda^{0.5}$ . *Lower panel:* Correlation between X-ray and lensing-inferred temperature  $k_B T_{\text{lens}} = \mu m_H \sigma_v^2$  (black diamonds) for CI-03, CI-05, CI-07, CI-14 and XLSSC44. The results of Cypriano et al. (2004) on massive clusters are reported for comparison (red stars) as well as those of Bardeau et al. (2006) (green crosses). The bisectrix line (dotted) represents energy equipartition between hot ICM gas and dark matter + galaxies collisionless fluid.

keV, the gas is hotter than expected by pure gravitational effects. This supports the presence of off-equilibrium physical processes (unrelaxed clusters, merging) as efficient sources of gas heating by shocks. Therefore this latter process enhances the X-ray temperature and luminosity of massive systems. But one has also to consider the possible bias introduced by cooling flows in some X-ray luminous clusters which could act to opposite way.

On the other side gas physics dominated by stellar formation and AGN processes are expected to dominate for less massive haloes like galaxies and groups and off-equilibrium processes to be insignificant. If present these astrophysical sources of gas heating/cooling are below the measurement errors of this present work.

Thanks to the availability of photometric redshifts for a large sample of background lensed sources it is possible to test whether cluster members decrease shear signal and bias  $\kappa$ -

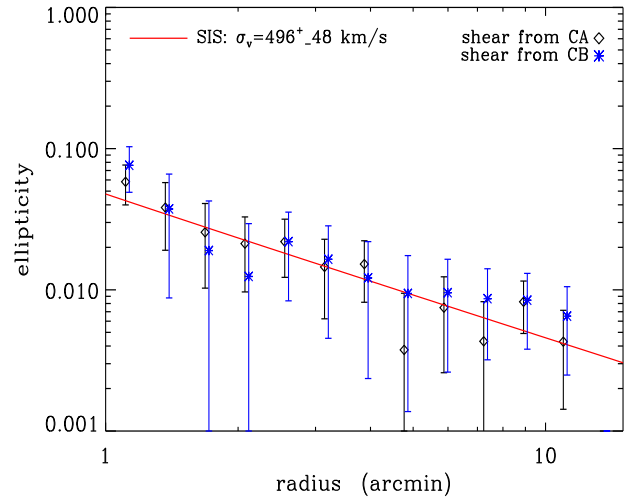


**Fig. 10.** Average radial shear profile for CI-03, CI-05, CI-07 and XLSSC44 at similar redshift  $z \sim 0.28 \pm 0.04$  and temperature  $T_X \sim 1.45 \pm 0.33 \text{ keV}$ . The mean velocity dispersion found by fitting a SIS profile is  $\sigma_v = 496 \pm 48 \text{ km s}^{-1}$ . There is no significant difference between the shear profile measured in source catalogue CA and source catalogue CB with  $z_{\text{phot}} > 0.5$ . This suggests that cluster members do not significantly reduce the shear profile and therefore affect detection efficiency. Points relative to CB catalogues are shifted rightward by 2% for clarity.

peak statistics. It has been shown that unlensed cluster member galaxies may significantly lower the shear profile around massive clusters (e.g. Broadhurst et al. 2005), and even change its shape if the contamination is not radially homogeneous. This so-called source-lens clustering effect (hereafter SLC), has been studied for large scale weak lensing (Bernardeau 1998; Hamana et al. 2002) and its implication for high order statistics of the convergence field (skewness and kurtosis). SLC should presumably be an important concern for a blind weak lensing cluster survey since the sample of background sources is necessarily contaminated by the galaxies of the clusters we aim at detecting. SLC effect is stronger for massive cluster lenses (since richness somehow scales like the mass) and for high redshift lenses. In order to give some hints on the amount of SLC contamination in the present WLCS, we measured the mean radial shear profile around peaks CI-03, CI-05, CI-07 and XLSSC44 which have similar properties ( $\sigma_v \sim 500 \text{ km s}^{-1}$ ,  $T_X \sim 1.5 \text{ keV}$  and  $z_1 = 0.28$ ) and are secure cluster detections coincident with X-ray sources from the XMM/LSS catalogue. If present we expect the SLC effect to have a similar strength for all of them. In Fig. 10 we show the mean shear profile around the four clusters when considering successively the source catalogue CA (with no photometric redshift information) and the source catalogue CB with photometric redshifts  $z_{\text{phot}} > 0.5 \gg z_1 = 0.28$ . In this latter case we expect no contamination. Fig. 10 shows that there is no significant difference between these two shear profiles. Both of them are consistent with a Singular Isothermal Sphere profile with velocity dispersion  $\sigma_v = 496 \pm 48 \text{ km s}^{-1}$ . The overall amplitude of the shear profile suggests that the redshift distributions of CA and CB catalogues are quite similar because the  $z_{\text{phot}} > 0.5$  cut in CB is balanced by lower limiting

magnitude cuts. Since these four clusters are characteristic of the bulk of our  $\kappa$ -peaks catalogue we can argue that SLC effect is kept at a low level in our analysis. However we expect this effect to be more pronounced in the shallower Wide survey containing massive and/or higher redshift haloes (Hamana et al. 2002). More quantitative predictions are beyond the scope of this analysis and should be addressed with numerical simulations with associated mock galaxy catalogues.

### 6.3. Merits of lens tomography

It is instructive to compare redshift estimates arising from lens tomography and from a direct excess of deflecting galaxies (*i.e.* cluster members identified by their photometric redshift). It is not a surprise that most WLCSs detections peak at  $\langle z_{\text{tom}} \rangle \simeq \langle z_{\text{phot}} \rangle \simeq 0.25$  because it corresponds to the redshift range in which gravitational lensing is most efficient for the source population we are considering.

In Fig. 11 we plot the comparison between these two redshift estimates for the 8 clusters having a well identified optical counterpart (namely clusters Cl-01, Cl-02, Cl-03, Cl-05, Cl-07, Cl-08, Cl-12 and Cl-14). Although the statistic is quite small and errors on  $z_{\text{tom}}$  are large, there is a rough correlation between both redshifts which is very encouraging. In addition we see in table 2 that among the five peaks with no tomographic redshift ( $z_{\text{tom}} = 0$ ) four are likely false detections with no optical counterpart. Therefore tomography can help eliminating such cases although for some other false detections (*i.e.* Cl-03) tomography provides a redshift estimate.

In order to improve this correlation, it will be important to improve the quality of photometric redshifts, especially for the distant background sources. It is not clear how much the catastrophic redshifts in the CB catalogue perturb lens tomography, but certainly for precision tomographic redshift estimates it will be important to increase the number of filters for photometric redshifts, especially in infrared bands (Bolzonella et al. 2000). In addition, it is noteworthy that our sample is made of low mass clusters ( $\sigma_v \sim 500 \text{ km s}^{-1}$ ), for which lens tomography does not provide valuable redshifts. For massive clusters, like those expected in the CFHTLS-Wide survey, the method will greatly gain in accuracy and reliability (Hennawi & Spergel 2005).

## 7. Conclusion

In this work we attempted to analyse the weak lensing signal in the 4 deg<sup>2</sup> images of the CFHTLS Deep fields. We resume the main points of this analysis

- For a proper signal extraction we paid special attention to the removal of residual systematics and got a large sample of distant lensed sources, thanks to the exceptional depth of the images. We then used standard KS93 inversion technique to infer the projected surface mass density (*i.e.* the convergence field) and focused on maxima peaks with a signal-to-noise ratio  $\nu > 3.5$ . We found 14 such peaks and discussed the possibility to use the statistics of maxima

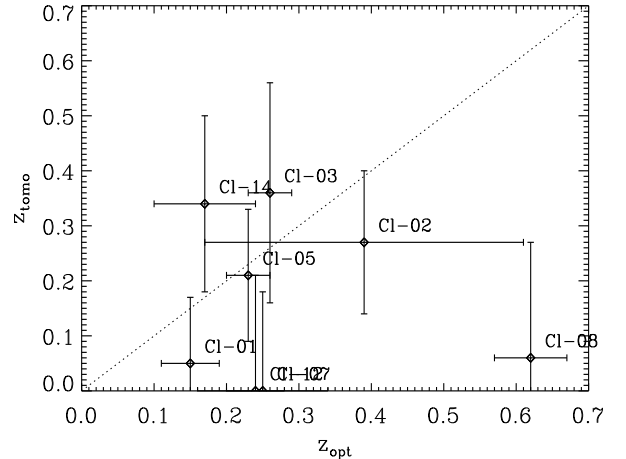


**Fig. 11.** Comparison between lens tomography and direct photometric redshift methods to estimate the redshift of the  $\nu > 3.5$   $\kappa$ -peaks. Only those peaks with a clear optical counterpart are included in the figure. Cl-02 as  $z_{\text{opt}} = 0.39$  is present although it might be the projection of several structures along the line of sight (thus explaining the broad error bar).

peaks as a test for the non gaussianity of the convergence field.

- We looked for an excess of galaxies around these peaks in order to check the validity of our galaxy cluster detections. We found that half of the  $\nu > 3.5$  cluster candidates are likely false or inconclusive detections without any clear optical counterpart. However projection effects are important even at high significance detection thresholds (see the case of Cl-02 and Cl-14).
- Our sample of secure detections is essentially made of low mass clusters with velocity dispersion  $\sigma_v \sim 500 \text{ km s}^{-1}$ . For the D1 field, we also compared the X-ray and lensing properties of the intersection of our sample and the XMM/LSS cluster survey and found a good sample matching. An interesting comparison between lensing and X-ray temperatures shows that our shear-selected clusters settle well on the bisectrix  $T_X = T_{\text{lens}}$  whereas more massive published systems suggest non-gravitational gas heating.
- We used lens tomography around  $\kappa$ -peaks to estimate the deflector redshift as well as its velocity dispersion. To this end we made an extensive use of photometric redshifts in the sample of background sources. In practice, the benefit of using tomography is rather low here because we are working on low mass systems. For massive clusters the use of a tomographic matched filter will increase the sensitivity of WLCS at high redshift (Hennawi & Spergel 2005).
- The Source-Lens Clustering effect (contamination of the background source catalogue by foreground unlensed cluster members) does not significantly affect our detections. This might not remain true for shallower surveys nor for higher redshift clusters.

Although the field area of the CFHTLS Deep survey is not wide enough for cosmological application, we have demonstrated that CFHTLS image quality is well suited for WLCSs

as it is the case for cosmic shear signal extraction (Semboloni et al. 2006). The full implementation of this technique to the CFHTLS Wide survey is on-going and will provide us with a few hundred shear-selected clusters. The large sky coverage will balance the lower density of background sources as compared to the Deep fields and will clearly favor the detection of higher mass systems with velocity dispersion in the range  $700 - 1200 \text{ km s}^{-1}$ . In addition half of this survey (the W1 region) will also be covered by the XMM/LSS survey. This will give the necessary calibration of scaling relations between mass and direct observables for clusters of galaxies to be used as efficient cosmological probes. A more detailed comparison with the performances of ongoing other clusters survey techniques (optical, SZ with Planck) will also become possible. The low completeness of WLCSs is balanced by the well controlled selection function of WLCSs since they require cosmological simulations with relatively low resolution and essentially no gas physics.

The opposite approach is also possible. We mentioned in Sect. 4.2 that it would be more interesting to use the statistics of  $\kappa$ -peaks as a test of the non Gaussianity of the convergence field. This contains complementary information on cosmological parameters relative to the cosmic shear 2-point correlation function. Like *e.g.* the skewness it helps breaking the observed degeneracy between  $\Omega_m$  and  $\sigma_8$  with shear correlation functions. In this respect it is not necessary to check whether individual peaks are real or false detections nor to assign a redshift and mass with expensive follow-up for each convergence peak.

Both WLCSs (with cluster identifications) and raw  $\kappa$ -peaks statistics are complementary applications of weak gravitational lensing. They both will soon provide new insightful constraints on the evolution of large-scale structure driven by Dark Matter and perhaps giving important clues on the behaviour of Dark Energy as a function of redshift.

*Acknowledgements.* We are thankful to R. Pelló and F. Ienna for making photometric redshifts available and for useful comments on their handling. We acknowledge fruitful discussions with C. Benoist, A. Blanchard, C. Marmo and L. Olsen. RG is supported at LATT by a postdoctoral contract #1019 from the CNRS. We thank the Programme National de Cosmologie of the CNRS for financial support.

## References

- Allen, S. W. 1998, MNRAS, 296, 392
- Arabadjis, J. S., Bautz, M. W., & Arabadjis, G. 2004, ApJ, 617, 303
- Arnaud, M. & Evrard, A. E. 1999, MNRAS, 305, 631
- Arnaud, M., Pointecouteau, E., & Pratt, G. W. 2005, A&A, 441, 893
- Astier, P., Guy, J., Regnault, N., et al. 2006, A&A, 447, 31
- Bahcall, N. A. & Bode, P. 2003, ApJ, 588, L1
- Bahcall, N. A., Lubin, L. M., & Dorman, V. 1995, ApJ, 447, L81+
- Bardeau, S., Soucail, G., Kneib, J. P., et al. 2006, in preparation
- Bartelmann, M., King, L. J., & Schneider, P. 2001, A&A, 378, 361
- Bartelmann, M. & Schneider, P. 2001, Phys. Rep., 340, 291
- Bernardeau, F. 1998, A&A, 338, 375
- Bertin, E. & Arnouts, S. 1996, A&AS, 117, 393
- Blanton, M. R., Hogg, D. W., Bahcall, N. A., et al. 2003, ApJ, 592, 819
- Bolzonella, M., Miralles, J.-M., & Pelló, R. 2000, A&A, 363, 476
- Borgani, S. & Guzzo, L. 2001, Nature, 409, 39
- Broadhurst, T., Takada, M., Umetsu, K., et al. 2005, ApJ, 619, L143
- Cabanac, R. A., Alard, C., Dantel-Fort, M., et al. 2006, in preparation
- Carlberg, R. G., Yee, H. K. C., Ellingson, E., et al. 1996, ApJ, 462, 32
- Carlstrom, J. E., Holder, G. P., & Reese, E. D. 2002, ARA&A, 40, 643
- Clowe, D., De Lucia, G., & King, L. 2004, MNRAS, 350, 1038
- Clowe, D., Schneider, P., Aragón-Salamanca, A., et al. 2006, A&A, 451, 395
- Cypriano, E. S., Sodr , L. J., Kneib, J.-P., & Campusano, L. E. 2004, ApJ, 613, 95
- da Silva, A. C., Kay, S. T., Liddle, A. R., & Thomas, P. A. 2004, MNRAS, 348, 1401
- Dahle, H., Kaiser, N., Irgens, R. J., Lilje, P. B., & Maddox, S. J. 2002, ApJS, 139, 313
- Dahle, H., Pedersen, K., Lilje, P. B., Maddox, S. J., & Kaiser, N. 2003, ApJ, 591, 662
- Das, S. & Ostriker, J. P. 2005, astro-ph/0512644
- De Filippis, E., Sereno, M., Bautz, M. W., & Longo, G. 2005, ApJ, 625, 108
- de Grandi, S., B hringer, H., Guzzo, L., et al. 1999, ApJ, 514, 148
- de Putter, R. & White, M. 2005, New Astronomy, 10, 676
- Eke, V. R., Cole, S., & Frenk, C. S. 1996, MNRAS, 282, 263
- Erben, T., Van Waerbeke, L., Bertin, E., Mellier, Y., & Schneider, P. 2001, A&A, 366, 717
- Gavazzi, R. 2005, A&A, 443, 793
- Gavazzi, R., Mellier, Y., Fort, B., Cuillandre, J.-C., & Dantel-Fort, M. 2004, A&A, 422, 407
- Geiger, B. & Schneider, P. 1998, MNRAS, 295, 497
- Gladders, M. D. & Yee, H. K. C. 2000, AJ, 120, 2148
- Gray, M. E., Taylor, A. N., Meisenheimer, K., et al. 2002, ApJ, 568, 141
- Haiman, Z., Mohr, J. J., & Holder, G. P. 2001, ApJ, 553, 545
- Haiman, Z., Wang, S., Khoury, J., et al. 2004, American Astronomical Society Meeting Abstracts, 205,
- Hamana, T., Colombi, S. T., Thion, A., et al. 2002, MNRAS, 330, 365
- Hamana, T., Takada, M., & Yoshida, N. 2004, MNRAS, 350, 893
- Hennawi, J. F. & Spergel, D. N. 2005, ApJ, 624, 59
- Hetterscheidt, M., Erben, T., Schneider, P., et al. 2005, A&A, 442, 43
- Heymans, C., Van Waerbeke, L., Bacon, D., et al. 2006, MNRAS, 350
- Hoekstra, H. 2003, MNRAS, 339, 1155
- Hoekstra, H., Hsieh, B. C., Yee, H. K. C., Lin, H., & Gladders, M. D. 2005, ApJ, 635, 73
- Hoekstra, H., Yee, H. K. C., & Gladders, M. D. 2004, ApJ, 606,

67

- Ilbert, O., Arnouts, S., McCracken, H. J., et al. 2006, *astro-ph/0603217*
- Jain, B. & van Waerbeke, L. 2000, *ApJ*, 530, L1
- Kaiser, N. & Squires, G. 1993, *ApJ*, 404, 441
- Kaiser, N., Squires, G., & Broadhurst, T. 1995, *ApJ*, 449, 460
- Kaiser, N., Wilson, G., Luppino, G., et al. 1998, *astro-ph/9809268*
- Kruse, G. & Schneider, P. 1999, *MNRAS*, 302, 821
- Mandelbaum, R., Tasitsiomi, A., Seljak, U., Kravtsov, A. V., & Wechsler, R. H. 2005, *MNRAS*, 362, 1451
- Maturi, M., Meneghetti, M., Bartelmann, M., Dolag, K., & Moscardini, L. 2005, *A&A*, 442, 851
- Mellier, Y. 1999, *ARA&A*, 37, 127
- Metzler, C. A., White, M., & Loken, C. 2001, *ApJ*, 547, 560
- Miralles, J.-M., Erben, T., Hämmerle, H., et al. 2002, *A&A*, 388, 68
- Miyazaki, S., Hamana, T., Shimasaku, K., et al. 2002, *ApJ*, 580, L97
- Olsen, L. F., Benoist, C., a, a., et al. 2006, in preparation
- Olsen, L. F., Scodreggio, M., da Costa, L., et al. 1999, *A&A*, 345, 681
- Padmanabhan, N., Seljak, U., & Pen, U. L. 2003, *New Astronomy*, 8, 581
- Pierre, M., Pacaud, F., Duc, P.-A., et al. 2006, *mNRAS* submitted
- Reblinsky, K. & Bartelmann, M. 1999, *A&A*, 345, 1
- Romer, A. K., Viana, P. T. P., Liddle, A. R., & Mann, R. G. 2001, *ApJ*, 547, 594
- Schirmer, M., Erben, T., Schneider, P., et al. 2003, *A&A*, 407, 869
- Schirmer, M., Erben, T., Schneider, P., Wolf, C., & Meisenheimer, K. 2004, *A&A*, 420, 75
- Schneider, P. 1996, *MNRAS*, 283, 837
- Seitz, C. & Schneider, P. 1997, *A&A*, 318, 687
- Semboloni, E., Mellier, Y., van Waerbeke, L., et al. 2006, *A&A*, 452, 51
- Starck, J.-L., Pires, S., & Réfrégier, A. 2006, *A&A*, 451, 1139
- Tang, J. Y. & Fan, Z. H. 2005, *ApJ*, 635, 60
- Taruya, A., Takada, M., Hamana, T., Kayo, I., & Futamase, T. 2002, *ApJ*, 571, 638
- Umetsu, K. & Futamase, T. 2000, *ApJ*, 539, L5
- Valtchanov, I., Pierre, M., Willis, J., et al. 2004, *A&A*, 423, 75
- van Waerbeke, L. 2000, *MNRAS*, 313, 524
- van Waerbeke, L., Mellier, Y., & Hoekstra, H. 2005, *A&A*, 429, 75
- White, M., van Waerbeke, L., & Mackey, J. 2002, *ApJ*, 575, 640
- Willis, J. P., Pacaud, F., Valtchanov, I., et al. 2005, *MNRAS*, 363, 675
- Wittman, D., Dell'Antonio, I. P., Hughes, J. P., et al. 2006, *ApJ*, 643, 128
- Wittman, D., Margoniner, V. E., Tyson, J. A., et al. 2003, *ApJ*, 597, 218
- Wittman, D., Tyson, J. A., Margoniner, V. E., Cohen, J. G., & Dell'Antonio, I. P. 2001, *ApJ*, 557, L89
- Wu, X. 2000, *MNRAS*, 316, 299